Session MP-2

Materials/Processes(2)

Effects of Plasma Cleaning on the Reliability of Wire Bonding (*Invited*)
J. M. NOWFUL, S. C. LOK, ASAT Ltd., Hong Kong
S.-W. Ricky LEE, Hong Kong University of Science & Technology, Hong Kong

Effects of Cu/Al Intermetallic Compound (IMC) on Copper Wire and Aluminum Pad Bondability
H. J. KIM, J. Y. LEE, K. W. PAIK, Korea Advanced Institute of Science and Technology, Korea
K. W. KOH, J. H. WON, S. H. CHOI, ASE Korea, Korea
J. LEE, J. T. MOON, Y. J. PARK, MK Electronics Co. Ltd., Korea

The Behavior of FAB(Free Air Ball) and HAZ(Heat Affected Zone) in Find Gold Wire
Sung-Jae HONG, Jong-Soo CHO, Jeong-Tak MOON, Jin LEE, MK Electronic Co. Ltd., Korea

Feasibility and Characterization Study of Al and Au Wire Bonding on Immersion Ag and Sn Coatings
W.K. SZETO, C.C. CHUM, Jang-Kyo KIM, Albert SZE, Y.M. CHEUNG, Hong Kong University of Science & Technology, Hong Kong

Effects of Particle Size on Dielectric Constant and Leakage Current of Epoxy/Barium Titanate ($BaTiO_3$) Composite Films for Embedded Capacitors
Sung-Dong CHO, Joo-Yeon LEE, Kyung-Wook PAIK, Korea Advanced Institute of Science and Technology, Korea

Effects of Plasma Cleaning on the Reliability of Wire Bonding

J. M. Nowful and S. C. Lok
ASAT Ltd.
QPL Industrial Building
Tsuen Wan, New Territories, Hong Kong

S.-W. Ricky Lee
Electronic Packaging Laboratory
Department of Mechanical Engineering
Hong Kong University of Science & Technology
Clear Water Bay, Kowloon, Hong Kong

Abstract

The yield of wire bonding predominantly depends on the surface characteristics of wire bond pads. The contamination on bond pads may result in low ball shear/wire pull strength and poor strength uniformity. Therefore, it is essential to remove the contaminants from the bond pad surface prior to wire bonding. In the present study, the effects of plasma cleaning on the reliability of wire bonding are investigated. Two types of plasma cleaning with various processing parameters are studied. Besides, specimens without plasma cleaning are also investigated for benchmarking. In addition to the comparison of contact angle, both ball shear and wire pull tests are performed to evaluate the effects of plasma cleaning. From the experimental data, it is observed that the plasma cleaning with proper parameter tuning can improve the contact angle characteristics and the reliability of wire bonding. However, a certain type of plasma cleaning may reduce the ball shear strength. Further analytical inspection is conducted on the bond pad surface. Detailed composition characterization is performed to confirm the findings of the present study.

Introduction

Wire bonding is the major interconnecting method between the die and the substrate. Since there are a tremendous amount of wires bonded in the electronic packages, the requirement for the yield and reliability of wire bonds is very high. For failure prevention and cost reduction, the processing parameters of wire bonding must be optimized to make reliable bonds [1].

In addition to obvious bonding parameters such as ultrasonic energy, time, force and temperature, there is another category of factors contributing to the success of wire bonding. They are the surface characteristics of bond pads [2]. In fact, the yield of wire bonding predominantly depends on the cleanness on the surface of bond pads. The contamination on bond pads may result in low ball shear/wire pull strength and poor strength uniformity. Therefore, it is essential to remove the contaminants from the bond pad surface prior to wire bonding.

In the literature, it is known that contaminants such as oxides and hydrocarbons can degrade the surface quality causing high wire bond failure rates. The contamination at a concentration level of less than one gram per cubic meter can already affect the bonding strength substantially. The source of contamination usually originates from the IC fabrication and package assembly processes. For instance, the residues from die singulation or outgassing from adhesives are potential contaminants [3]. A proper cleaning process may remove the unwanted particles and enlarge the process windows of wire bonding. As a result, the bonding quality is improved and the production yield is increased. However, conventional cleaning methods such as wet chemical cleaning and solvent degreasing have the drawback that the traces of chemicals are left on the treated surface. Therefore, they have often been found to be inadequate for the complete removal of contaminants [4]. Nowadays there are various approaches to reduce the contamination on organic and metallic surfaces. Among them, the plasma cleaning technology is considered the most promising one.

In the present study, the effects of plasma cleaning on the reliability of wire bonding are investigated. Two types of plasma cleaning with various processing parameters are studied and compared to specimens without plasma cleaning. After the surface treatment on the wire bond pads, the contact angle is measured as an index of the surface quality. Subsequently, both ball shear and wire pull tests are performed to evaluate the effects of plasma cleaning. Furthermore, a detailed surface analysis using Auger electron spectroscopy (AES) is conducted on the bond pad surface. The composition on the surface with various treatments is characterized to interpret the results of the present study.

Plasma Cleaning

Many gases may become reactive at a certain temperature. However, with the activation of electrons, some gases may achieve reactivity in plasma at the room temperature [5]. The plasma cleaning is performed in a vacuum chamber (see Figure 1) that is equipped with an insulated substrate holder. Magazines filled with strips are placed on the strip holder. The plasma source consists of a heated filament placed in a separate cavity. An orifice connects the cavity to the chamber. A working gas (usually Ar gas) is fed in to the cavity. For cleaning, the reactive gas (H_2) is fed directly into the vacuum chamber. A gas discharge is established by applying a potential between the heated filament and ground. For the DC voltage of 20-30V, electron currents between 10A and 200A are obtained from the plasma source using a power supply. The hydrogen gas is activated (or ionized) with the DC discharge [5]. The energy of activated gas is large enough to enhance the gas–surface chemistry to form hydrogen volatile compounds, but still too small to remove materials by physical impact (sputtering). Therefore, the re-deposition of particles is avoided.

Figure 1: Plasma Machine for Reactive Cleaning

Figure 2: Plasma Machine for Sputtering Cleaning

The aforementioned mechanism may be called plasma chemical cleaning or reactive cleaning. There is another type of plasma machine using a different mechanism for cleaning. When the bias voltage applied to the substrate is larger than a specific threshold, high energetic ions are generated to perform cleaning by removing surface particles, in particular, non-volatile species such as metal atoms, with physical impact (sputtering). For instance, the sputtering threshold for Cu, Ni and Al is 17eV, 21eV and 13eV, respectively. This type of cleaning mechanism may be called plasma physical cleaning or sputtering cleaning (see Figure 2).

Compared to plasma chemical cleaning, plasma physical cleaning has a serious drawback that a portion of the sputtered, non-volatile particles may be floating around inside the processing chamber and re-deposited back to the specimens under cleaning. This phenomenon may increase the risk of cross-contamination, especially when different types of substrate materials are processed in the same cleaning chamber. Furthermore, on metallic surfaces, plasma physical cleaning does not have the feature of self-terminating as plasma chemical cleaning does [5]. Therefore, there may be a risk of "over-cooking".

Table 1: Matrix for Design of Experiment

DOE Leg #		Cleaning Time	Gas Ratio	RF Power
1 (no plasma)		-	-	-
2 (Reactive Plasma Cleaning)	a	5 min	20:20	-
	b	5 min	20:40	-
	c	10 min	20:20	-
	d	10 min	20:40	-
3 (Sputtering Plasma Cleaning)	a	10 sec	-	400
	b	10 sec	-	500
	c	20 sec	-	400
	d	20 sec	-	500

Experimental Procedures

In the present study, all specimens were GaAs die with Al bond pads. Besides, the dies had been attached to Ag plated Cu leadframes. For the purpose of design of experiment (DOE), a test matrix with 9 legs as shown in Table 1 was arranged. Two types of plasma treatment (reactive type: Balzer LFC 150 and sputtering type: Panasonic PC30) with various processing parameters were performed to clean the bond pads before wire bonding. Besides, specimens without plasma cleaning were also investigated for benchmarking.

After the surface treatment, the contact angle was measured as an index of surface quality of the bond pads. Subsequently, Au wires were bonded to the treated pads using ESEC 3006 high frequency (128 kHz) ball bonder. The wire diameter and the bond pad pitch were 1.2 mils and 80 µm, respectively. In order to evaluate the effects of plasma cleaning, both ball shear and wire pull tests were conducted using a DAGE tester. Furthermore, AES analysis was performed on the treated, but not bonded, pad surface. The composition on the surface was characterized to interpret the results of the present study.

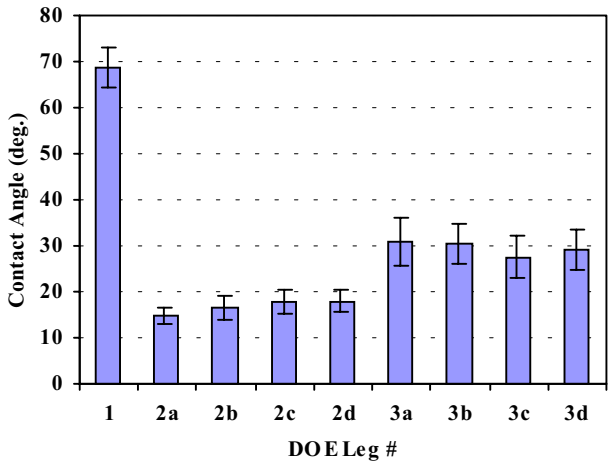

Figure 3: Comparison of Contact Angle

Testing Results and Discussion

Contact angle measurement

The contact angle method is widely used to characterize the wetting quality of a surface. Such measurement is a simple index to describe how easy (or how difficult) a certain liquid can wet a particular surface. In general, a contact angle less than 90^{o} would represent a wettable surface. Otherwise, the surface is considered non-wettable [6].

In principle, high surface energy solids are hydrophilic and tend to promote wetting. Conversely, low surface energy solids, which do not promote wetting, are hydrophopic. Since most organic contaminants are hydrophopic, the measurement of contact angle can serve as a simple method to characterize the surface cleanness of wire bond pads.

In the present study, the contact angle measurement was performed using Glassivation before (Leg #1) and after (Legs #2 and #3) plasma cleaning. The measurement results are presented in Figure 3. Note that the mean and standard deviation values in Figure 3 are based on a testing population of 20 samples for each case. It is observed that the surface without plasma cleaning has a contact angle of 68^{o}; the surface with reactive plasma cleaning has a contact angle of ~17^{o}; the surface with sputtering plasma cleaning has a contact angle of ~28^{o}. In other words, from the results of contact angle measurement, the surface cleanness of bond pads is in the order of plasma chemical cleaning (best), plasma physical cleaning, and no plasma cleaning (worst). Note that, among different cases within Leg #2 and Leg #3, respectively, the variation in contact angle is not significant.

Ball shear strength

The ball shear strength is the most direct index to evaluate the quality of ball bonds. The testing results for all nine cases are given in Figure 4. Note that the mean and standard deviation values in Figure 4 are based on a testing population of 25 samples for each case. The general trend indicates that the specimens with reactive plasma cleaning have the highest ball shear strength. Also, it is interesting to note that the bond pads with sputtering plasma cleaning have a lower ball shear strength than those without any plasma treatment. It is believed that this phenomenon is due to the "secondary contamination" caused by the re-deposition of sputtered particles. It is also observed that, for various cases within Leg #2 and Leg #3, the ball shear strength may be affected by the processing parameters. Therefore, the proper tuning of plasma cleaning is essential to the bonding quality.

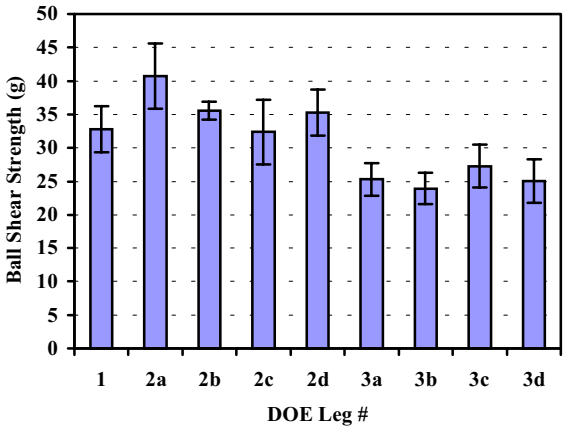

Figure 4: Comparison of Ball Shear Strength

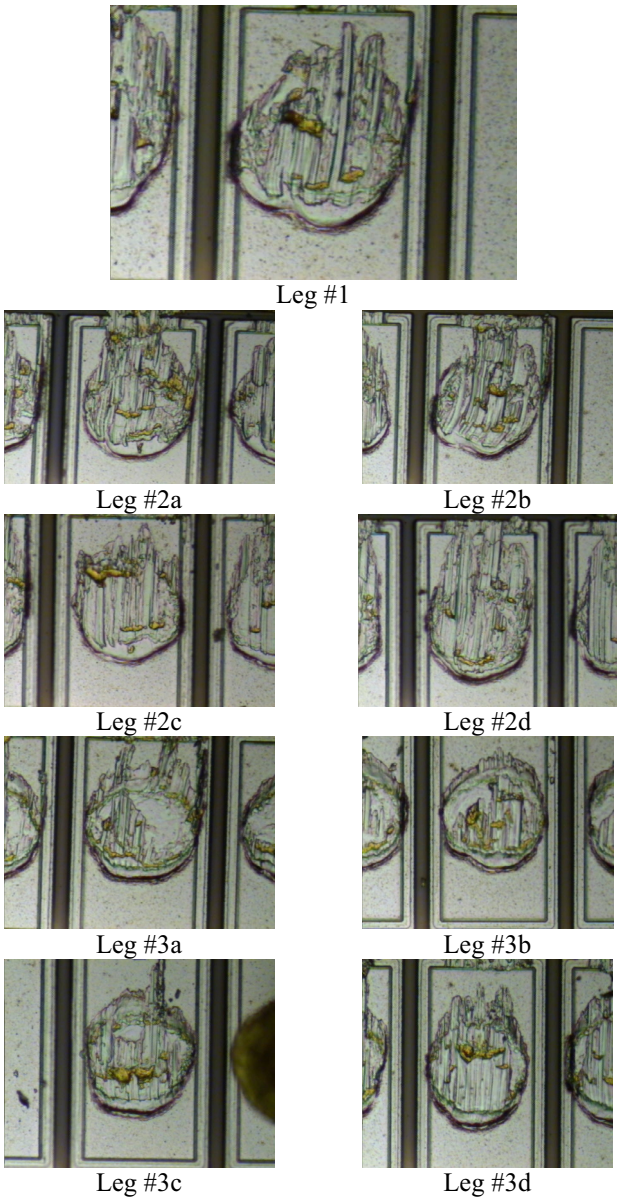

Figure 5: Comparison of Post-Ball Shear Pattern

Furthermore, optical microscopy was performed on the tested bond pads to inspect the failure modes. From the pictures shown in Figure 5, it is noted that the post-ball shear failure modes of Leg #1 and Leg #3 are similar. On the other hand, the specimens subjected to reactive plasma cleaning show a pattern with more "dragging", which is considered a sign of higher ball shear strength.

Wire pull strength

In the present study, in addition to the ball shear test, the wire pull test was also conducted to evaluate the effects of plasma cleaning. The testing results are shown in Figure 6. Note that the mean and standard deviation values in Figure 6 are based on a testing population of 25 samples for each case. In general, the deviation in the wire pull strength among various cases under investigation is not significant. However, more detailed comparison reveals that the standard deviation of Leg #1 data is larger than others indicating a poorer wire pull strength uniformity. Furthermore, it is found that the wire

pull strength is still the lowest among the three legs. This phenomenon should be due to the effect of particle re-deposition as explained in the previous section.

Figure 7 presents the optical microscopy on the top of ball bonds after wire pull test. It is observed that Leg #1 and Leg #2 have similar failure (neck breaking at the top of ball bond). Nevertheless, some specimens in Leg #3 show a failure mode of ball bond lift-off. This observation confirms that the lower wire pull strength of Leg #3 is a result of poor ball bonding, which should be due to the "secondary contamination" [7].

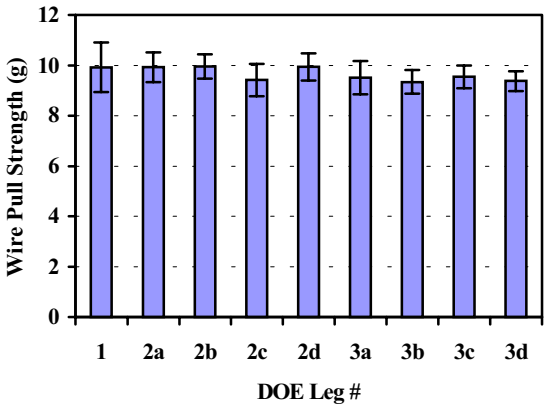

Figure 6: Comparison of Wire Pull Strength

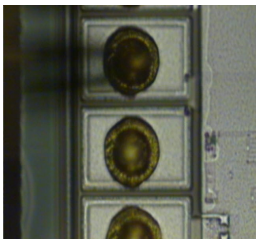

No Plasma Cleaning
(neck breaking)

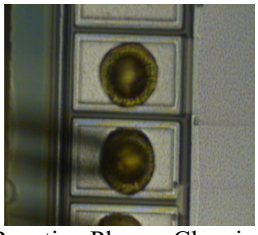

Reactive Plasma Cleaning
(neck breaking)

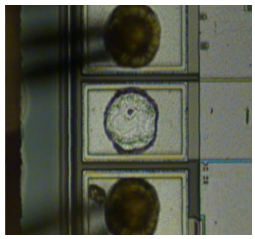

Sputtering Plasma Cleaning
(ball bond lift-off)

Figure 7: Comparison of Post-Wire Pull Pattern

Table 2: AES Analysis for Pad Surface Composition

DOE #	C	O	Al	F	Cu	Ag
1	33.7	26.5	39.8	-	-	-
2a	9.7	47.9	42.4	-	-	-
2b	8.4	48.9	40.7	2.1	-	-
2c	9.8	49.0	38.7	2.5	-	-
2d	8.2	50.1	40.4	1.4	-	-
3a	20.6	34.2	38.5	-	4.4	2.3
3b	7.9	38.6	35.0	-	15.3	3.1
3c	8.6	34.1	38.7	-	14.3	4.4
3d	10.8	29.0	38.3	-	16.7	5.3

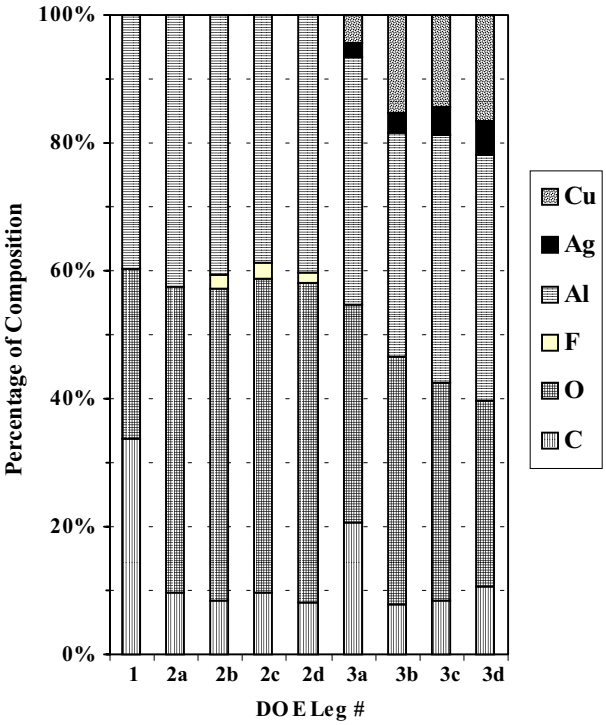

Figure 8: AES Surface Analysis

AES Surface Analysis

In order to investigate the re-deposition effect, a surface analysis using AES was performed on treated bond pads without wire bonding. From the surface composition analysis shown in Figure 8, it is observed that the plasma cleaning (both reactive and sputtering types) could effectively remove organic (corresponding to the carbon concentration) contaminants [8]. However, for those specimens in Leg #3, new contaminants such as Ag and Cu were introduced. It is believed that these elements were sputtered particles from the leadframe. Those particles were floating around inside the cleaning chamber and eventually re-deposited to the surface of specimens, causing poorer wire bonding strengths (including ball shear and wire pull).

In Figure 8, it should be noted that there is a small amount of fluorine (F) detected on the specimens in Legs #2b-2d. It seems that this extra element has some impact on the wire bonding quality (because #2a is always the best case among Leg #2 in Figures 4 and 6). However, the source of fluorine is not yet determined.

Summary and Conclusions

In this paper, an investigation on the effects of plasma cleaning on wire bonding is presented. Both reactive and sputtering types of plasma cleaning with various processing parameters were studied and compared to specimens without plasma cleaning. For design of experiment, a test matrix with nine different cases was arranged. During the course of the present study, several experimental techniques were applied to evaluate the effects of plasma cleaning. Among them were contact angle measurement, ball shear test, and wire pull test. Furthermore, an AES surface analysis was conducted to interpret the results of the present study.

From the comparison of contact angle, it was observed that the plasma cleaning could substantially improve the wetting ability of the bond pad surface. The experimental data from both ball shear and wire pull tests indicated that, compared to the bond pads without plasma treatment, the reactive plasma cleaning could provide the highest wire bonding strength but the sputtering plasma cleaning would in fact reduce the wire bonding strength. Further failure analysis by optical microscopy also confirmed the aforementioned phenomena.

With the AES analysis, the composition on the surface of bond pads for all cases under investigation was characterized. It was identified that both types of plasma cleaning could effectively remove organic contaminants. However, for those specimens with sputtering plasma treatment, new contaminants were introduced inside the cleaning chamber and eventually re-deposited to the surface of specimens. As a result, the wire bonding strengths (including ball shear and wire pull) were reduced.

In conclusion, the bond pads with reactive plasma cleaning can provide the best wire bonding quality. However, with various processing parameters, there is still some deviation in bonding strength. Therefore, it is essential to optimize the processing parameters of reactive plasma cleaning so that the highest yield and reliability of wire bonding can be achieved.

References

1. George G. Harman, Wire Bonding in Microelectronics: Materials, Process, Reliability and Yield, 2nd edition, McGraw-Hill (New York, 1997)
2. Cai, J., Lee, S.-W.R., Lau, D. and Leuenberger, E., "Effects of Surface Characteristics on the Bondability of PBGA Soft Au Wire Bond Pad," *Proc. 3rd International Symposium on Electronic Packaging Technology (ISEPT)*, Beijing, China, August 1998, pp. 176-181.
3. James L. Jellison, "Kinetics of Thermo-compression Bonding to Organic Contaminated Gold Surfaces," *Proc. Electronic Components Conference*, 1976, pp. 92-97.
4. Bushmire, D. W. and Holloway, P. H., "The Correlation between Bond Reliability and Solid Phase Bonding Techniques for Contaminated Bonding Surfaces," *Proc. International Microelectronics Symposium (ISHM),* Orlando, Florida, October 1975, pp. 402-407.
5. Nico Onda, Zeno stossel, Alex Dommann and Jurgen Ramm, "DC Hydrogen Plasma Cleaning: A Novel Process for IC Packaging," *Proc. Semicon-West*, San Jose CA, July 1997.
6. Schneuwly, P.Groning, L.Schlapbach, and V.P.Jackelin, "Influence of Surface Contamination on Metal/Metal Bond Contact Quality," *Journal of Electronic Materials*, Vol. 27, No. 8 (1998), pp. 990–999.
7. Dini, J. W., and Johnson, H. R., "Influence of Codeposited Impurities on Thermo-compression Bonding of Electroplated Gold," *Thin Solid Films*, Vol. 45 (1977), pp. 59-68.
8. Casey, D. J., and Endicott, D. W., "Control of Surface Quality of Gold Electrodeposits Utilizing Auger Electron Spectroscopy," *Plating and Surface Finishing*, Vol. 67 (1980), pp. 39-42.

Feasibility and Characterization Study of Al and Au Wire Bonding on Immersion Ag and Sn Coatings

*W.K. SZETO, C.C. CHUM, Jang-Kyo KIM, #Albert SZE and #Y.M. CHEUNG
Department of Mechanical Engineering, Hong Kong University of Science & Technology
Clear Water Bay, Hong Kong. *E-mail: wkszeto@ust.hk
#ASM Assembly Automation Ltd., Kwai Chung, Hong Kong

Abstract

Immersion Ag and immersion Sn coatings obtained through the electroless process have emerged as an alternative to Ni/Au metallisation layer for more uniform thickness and lower material cost. Microscopic studies by SEM, AFM and TEM indicated that the Ag coating had a finer surface morphology and lower thickness than the Sn coating. Composition study by XPS indicated that copper and sulphur were present in the Ag coating surface, indicating migration of underlying copper layer and tarnishing of silver surface. Further study based on the D-SIM revealed that both the Ag and Sn immersion coatings were organometallic in nature.

Wire bond mechanical tests showed that both the Al and Au wires were bondable on immersion Ag finish. However, the bondability of these two wires on immersion Sn was poor due likely to low melting point of the Sn intermetallic. Further study is required to verify whether grain size and hardness of Sn finish would affect wire bondability. Plasma treatment and UV/Ozone treatment were made onto these plates with no appreciable improvement in bondability. Fracture analysis of the bonded Ag coating indicated that the wire broke at the neck after pull test, a reflection of lower strength of wire at the necked region than at the bonded interface, as also confirmed by the lower pull strength than the shear strength.

Introduction

Organic printed circuit boards (PCBs) with Ni/Au plates on bond pads have been widely used for interconnection in chip-on-board (COB), ball grid array (BGA) and chip-scale packages (CSP). With low cost as a driver in the electronic packaging industry, immersion coatings obtained through the electroless process have emerged as an alternative to Ni/Au metallisation layer. These coatings have advantages of uniform thickness and low material and processing costs compared to the conventional electrolytic Ni/Au metallisation layers for wire bonding. The previous study on wire bondability to immersion Ag was concentrated on optimization and fine tunning of wire bonding parameters [1]. Therefore, the use of the PCB with immersion Ag finish needs more detailed characterization studies before it can be extensively used [2]. For the use of PCB with even cheaper immersion Sn finish [3], careful studies are also required because this finish has been developed as an alternative to Sn/Pb finishes for solder joints [4,5] but not for wire bonding.

This paper is to characterize the AlphaLEVEL™ immersion Ag [6] and Dexcoat FST immersion Sn coatings [7], as well as to study the feasibility of using Al and Au wires for bonding onto these two finishes. Several state-of-the-art techniques and instruments, including scanning electron microscope (SEM), atomic force microscope (AFM). X-ray photoelectron spectroscopy (XPS), transmission electron microscope (TEM) and dynamic secondary ion mass spectrometry (D-SIM), were employed to measure the surface and elemental, physical and chemical characteristics of Ag and Sn coatings. Special emphasis was placed on establishing the correlations of the characteristics with wire bond strength. An AB559 automatic wedge bonder with ultrasonic transducer frequency at 62 kHz was employed to bond 32 μm Al wire and 25 μm Au wire onto the immersion coatings. After measurement of pull and shear strengths, microscopic analyses of the fracture surface were performed to identify the failure mechanisms.

The plasma treatment has been proved to be effective in removing organic contamination with improvement in the wire bondability on Au metallization [8]. Plasma and UV/Ozone treatments were also be performed on these coatings to observe any improvement in wire bondability.

Experiments & Results

The experiments were divided into four parts: characterization studies of the immersion coatings, mechanical wire bondability tests, fracture analysis of the bond pads after pull/shear tests and finally effects of plasma and UV/Ozone treatments on bondability.

Characterization Studies of Immersion Ag and Sn

Surface Morphologies by SEM

The SEM pictures taken by a JOEL scanning electron microscope are shown in Fig 1a & 1b. The immersion Ag coating has a finer grain structure than the immersion Sn coating. The Sn has a well polygonized grain structure which had been reported helpful to resist dendritic growth and whisker formation [3,9]. The grain size is believed to have a significant effect on solderability as well as on wire bondability because the soft, well-defined polygonized grain crystal [3] is easier to form intermetallics than those with irregular coarse grains of brittle and hard properties. Previous study on Au metallization had proved that hardness of substrate surface would affect wire bondability [8].

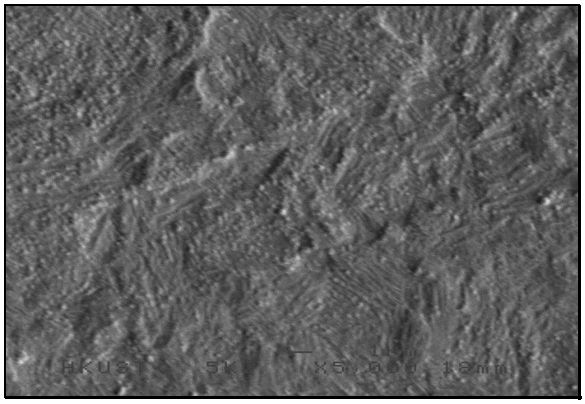

Fig 1a : SEM pictures of immersion Ag coatings at 5000X

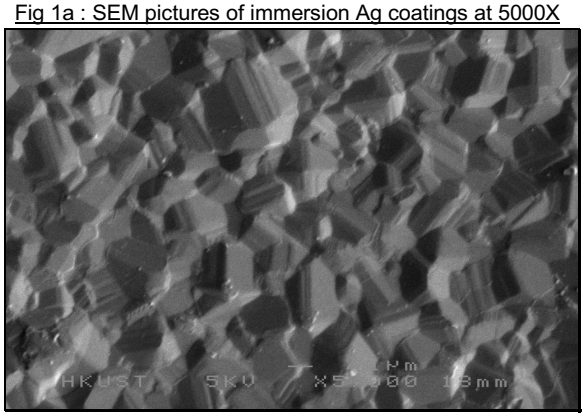

Fig 1b : SEM pictures of immersion Sn coatings at 5000X

Surface Morphologies & Roughnesses by AFM

The AFM images of Ag and Sn coatings were obtained from a scanned area of 100µm X 100 µm using Nanoscope E of Digital Instruments are shown in Fig 2a & 2b.

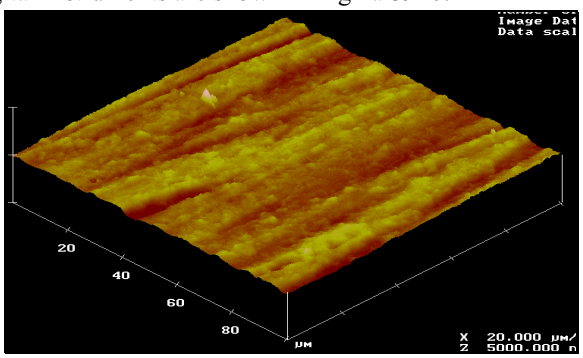

Fig 2a : AFM pictures of immersion Ag at 100µm X 100 µm scan area.

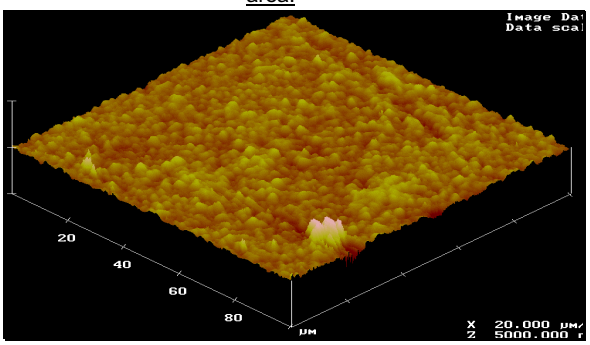

Fig 2b : AFM pictures of immersion Sn at 100µm X 100 µm scan area.

These AFM images are basically similar to those produced from SEM. The AFM can additionally produce the 3D images with roughness data determined in terms of the arithmetic mean (Ra) and root mean square (Rms) as follows :

$$R_a = \int_{-\infty}^{\infty} |z - m| dz \qquad \ldots\ldots\ldots\ldots\ldots\ldots \quad (1)$$

$$R_{rms} = \left[\int_{-\infty}^{\infty} (z^2) p(z) dz \right]^{\frac{1}{2}} \qquad \ldots\ldots\ldots\ldots\ldots\ldots \quad (2)$$

As indicated in Fig 3, the roughness of immersion Ag is lower than that of immersion Sn.

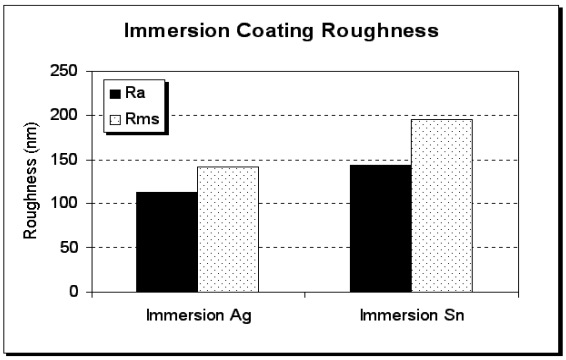

Fig 3 : Surface roughness of immersion coatings by AFM

Surface Compositions & Depth Profiling by XPS

The experiment was conducted using the PHI 5600 Multi-technique System. The XPS spectra of immersion Ag and Sn finishes are summarized in Fig 4a & 4b.

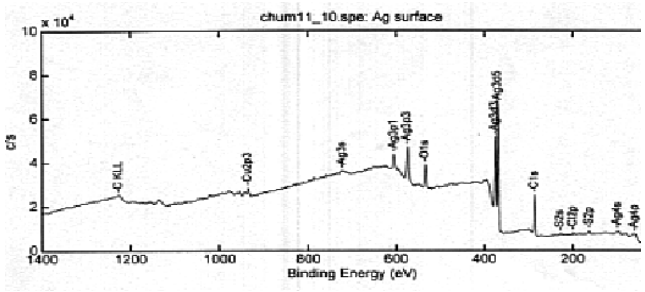

Fig 4a : XPS Spectrum of immersion Ag

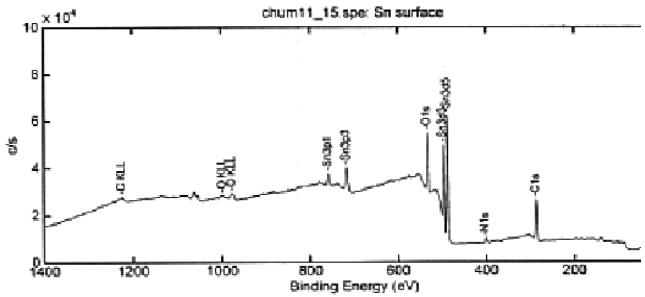

Fig 4b : XPS Spectrum of immersion Sn

By integration of the peak area, the elemental compositions of the coatings were determined as shown in Fig 5.

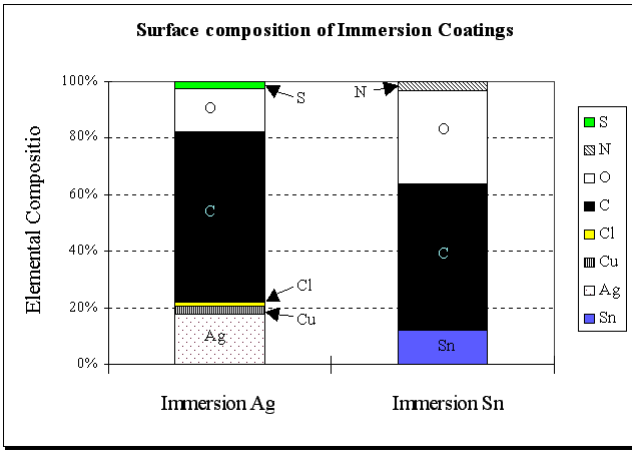

Fig 5 : Elemental Composition of the immersion Ag (left) and immersion Sn (right) at Surface by XPS

The presence of sulfur (S) on the Ag surface indicates that silver was tarnished due to reaction between Ag and the trace amount of sulphur dioxide in atmosphere. Copper (Cu) was also present arising probably from migration of the base Cu substrate. Sulfur was not found at the immersion Sn surface indicating that there was no tarnishing because Sn was not reactive with sulfur dioxide. Copper was also not observed proving that Cu migration was not significant for the Sn coating.

To better understand the elemental composition change across the whole layer of immersion coating, an XPS depth profiling was conducted for each coating, and the results are summarized in Fig 6a & 6b.

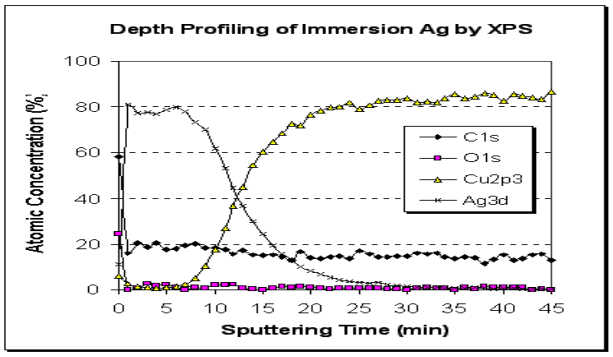

Fig 6a : Depth Profile of immersion Ag coating by XPS.

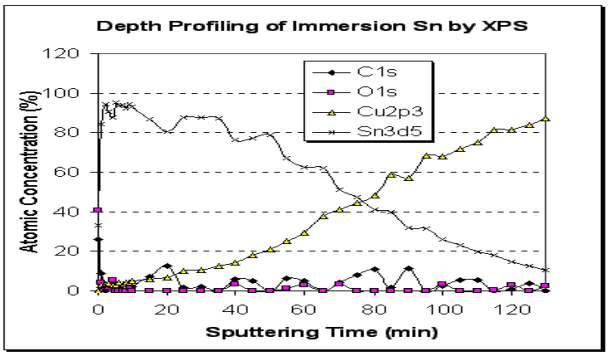

Fig 6b : Depth Profile of immersion Sn coating by XPS.

As observed from Fig 6a, the Cu content increased and the Ag content decreased with sputtering time for immersion Ag. Equilibrium values were attained at which the Cu base substrate was arrived. Similar drop of Cu content was also observed in Fig 6b, due to high coating thickness of immersion Sn, the base substrate was not reached within our experimental limit. The presence of O, C in both the coatings indicated the presence of organic ingredients.

Cross sectional structure by TEM [10]

The cross sectional TEM structures are shown in Fig 7a & 7b for the Ag and Sn coatings respectively. It could be observed from the TEM photos that immersion Ag had a lower coating thickness and much finer grain structure than immersion Sn.

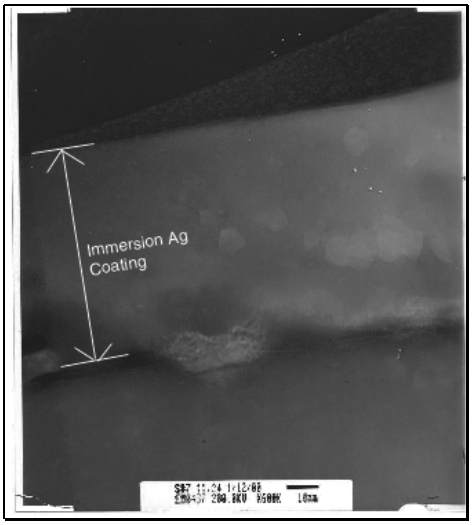

Fig 7a : Cross sectional structure of immersion Ag by TEM.

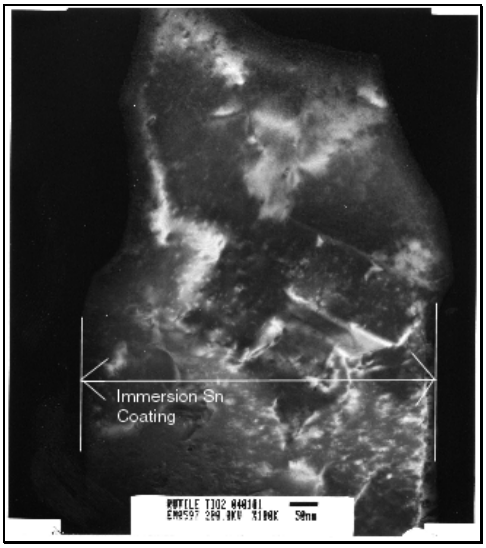

Fig 7b : Cross sectional structure of immersion Sn by TEM.

Cross sectional compositions by D-SIM

The test specimens were bombarded with a narrow beam of cesium ions, the secondary ions generated from the bombarded area were then separated according to their mass-

to-charge ratio. The relative quantity of the measured secondary ions were counted and converted to concentrations, to reveal the composition and trace impurity content of the the specimen as a function of sputtering time (depth) with result as summarized in Fig 8.

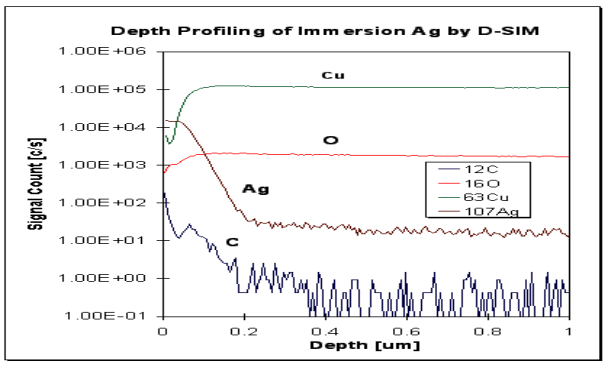

Fig 8a : Depth Profile of immersion Ag by D-SIM

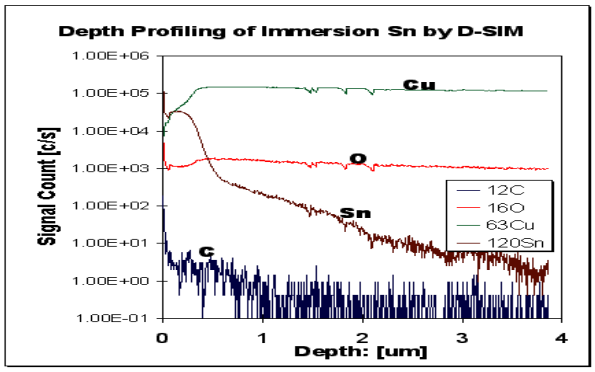

Fig 8b : Depth Profile of immersion Sn by D-SIM

Due to use of higher molecular weight of Cs+ ion, the penetrating power of D-SIM is higher than XPS. The D-SIM result agreed well with the XPS depth profiles in that the immersion Ag is thinner than Sn. Furthermore, the presence of C and O within the coating layer indicated that both the immersion coatings contained organic materials. The organic ingredients originated from organic additives added in the immersion solutions to improve the quality of coatings and to enhance operating window of immersion solutions [11].

Mechanical Bondability Test

An AB559 automatic wedge bonder was used to produce Al and Au wire ultrasonic wedge bonds to the Ag and Sn bond pads. Several bonding setups were tried for best bondability for each set of conditions. Table 2 lists the optimized bonding parameters achieved and utilized for the whole experiment.

It was observed that bonding could only be made on immersion Ag, but not on immersion Sn. To measure the wire bond strength on Ag coating, the pull and shear test were performed and the results are summarized in Fig 9. The pull test was conducted on a conventional pull tester, whereas shear test on a Dage Gauge 4000 at a shear height of 4µm.

Table 2 : Wire bonding setup

Bonding wire	Tanaka 1.25 mil Al wire	American Fine Wire 1 mil Au wire
Wedge tool:	Gaiser, 2130-2025-L	SPT, FP30B-TI-2020-L-CGM
Ultrasonic transducer	Uthe 70PTL wedge transducer (62 kHz)	
Heat-up Temp (•)	25	125
Bond power (unit)	100	85
Bond force (g)	20	20
Bond time(ms)	30	30

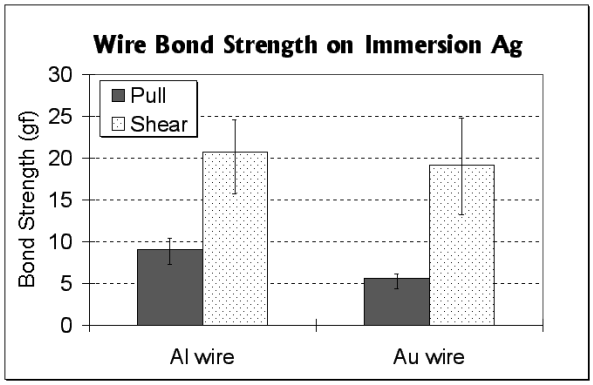

Fig 9 : Pull strength and shear strength of Al wire and Au wire on immersion Ag

As shown, both the pull and shear strengths of Al wire were higher than those of Au wire while the shear strength was much higher than pull strength for both wires.

Fracture Analysis

To better understand the fracture phenomenon and why shear strength was much higher than pull strength, a fracture analysis was performed before and after the test based on the microscopy. Fig 10 shows the normal view of the Al and Au wire bonds on immersion Ag.

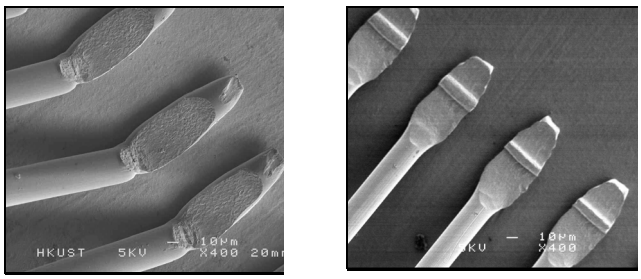

Fig 10 : Normal View of Wedge Bonding of Al wire (left) and Au wire (right) on immersion Ag by SEM

As shown in Fig 10, the wedge bond of the Al wire is different from Au wire due to difference in the design of wedge bond tools. It seems that the wedge bond tool for Al wire made a weak keel neck as this portion appeared to be very thin to break. It was then observed that debonding did occur at the keel neck for Al bond after pull test as shown in Fig 11. For Au bond, breaking occurred at the thin region of bond pad with the weakest strength. Therefore, pull strength

does not represent a real measure of the interfacial bond between the wire and the substrate as the bond pad deformed during the bonding thereby making the thin region with the weakest wire strength to break when pull test was performed.

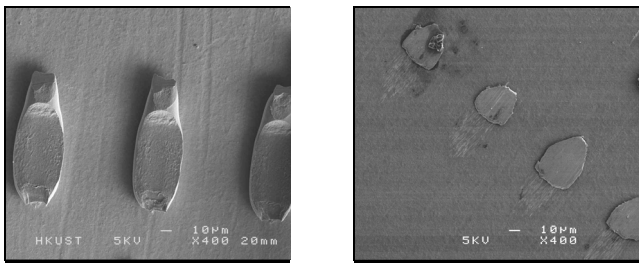

Fig 11: Substrate of immersion Ag after pull tests of Al wire (left) and Au wire (right)

To measure the actual wire bond strength, the shear test was performed, Fig 9 showing that the shear strength much higher than the pull strength. The fracture surface after the shear test is shown in Fig 12.

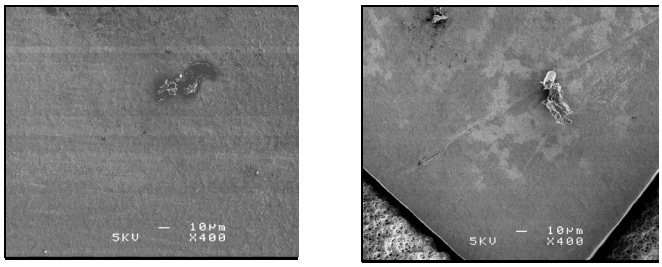

Fig 12 : Substrate of immersion Ag after shear tests of Al wire (left) and Au wire (right)

As shown, the substrate surface was only left with residue of wire material with almost the whole wedge bond removed. The fracture surface consistently exhibited failures at the bonded region, rather than failure at the wire neck. This suggests that the shear strength is a better representation of the interfacial wire bond strength.

Effect of Plasma Cleaning and UV/Ozone Cleaning

To study the effect of plasma [12] and UV/Ozone cleaning on wire bondability on immersion Ag and Sn, a study was performed with the as-received sample as control. After cleaning, the Ag substrate was analyzed using XPS to study the elemental changes on the surface. The pull strength and shear strengths were also measured.

The elemental compositions of the as-received, plasma-cleaned and UV/Ozone-cleaned Ag samples are shown in Fig 13.

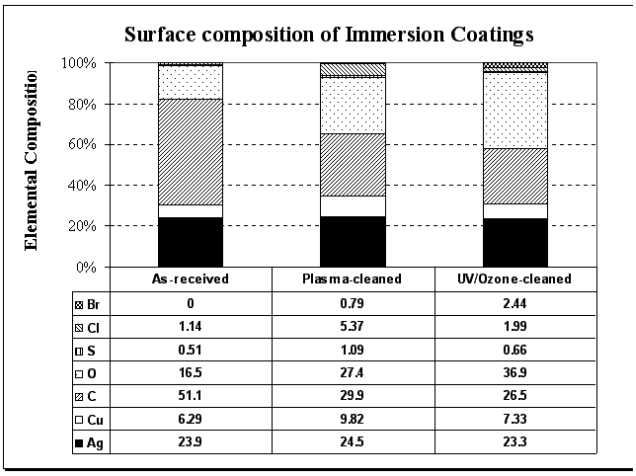

	As-received	Plasma-cleaned	UV/Ozone-cleaned
Br	0	0.79	2.44
Cl	1.14	5.37	1.99
S	0.51	1.09	0.66
O	16.5	27.4	36.9
C	51.1	29.9	26.5
Cu	6.29	9.82	7.33
Ag	23.9	24.5	23.3

Fig 13 : Elemental composition of the as-received, plasma-cleaned and UV/Ozone-cleaned immersion Ag samples analysed by XPS

As illustrated in Fig 13, the carbon content dropped significantly after either plasma cleaning or UV/Ozone cleaning. This indicated that organic contamination was somehow removed. However, the oxygen content increased at the same time, indicating that the substrate surface was also oxidized after the cleaning. Furthermore, the sulphur content increased after cleaning due to tarnishing, and the copper content increased due probably to accelerated migration from the underlying Cu during cleaning.

The wire bondability results are summarized in Table 3. Either plasma or UV/Ozone cleaning did not improve the bondability for Sn coating, although there was some improvement for Au wire on Ag coating after UV/Ozone cleaning. The Al wire bond strengths before and after cleaning on Ag coatings are shown in Fig 14. It shows that there was no significant change on pull strength as expected because the wire broke at the heel neck of the wire, not at the interface of the bonding. There was no significant change in shear strength after plasma cleaning, and worse still, there was a drop in shear strength after UV/Ozone cleaning, due probably to oxidation and tarnishing as verified by the XPS analysis in Fig 13.

Table 3 : Summary of Bondability before and after Treatment

* Only 70 % success rate for Au wire bonding on the UV ozone cleaned immersion Ag pad.

	Immersion Ag		Immersion Sn	
	Al wire	Au wire	Al wire	Au wire
As-received	*Succeed*	*Failed*	*Failed*	*Failed*
Plasma-cleaned	*Succeed*	*Failed*	*Failed*	*Failed*
UV/Ozone-cleaned	*Succeed*	* *Succeed*	*Failed*	*Failed*

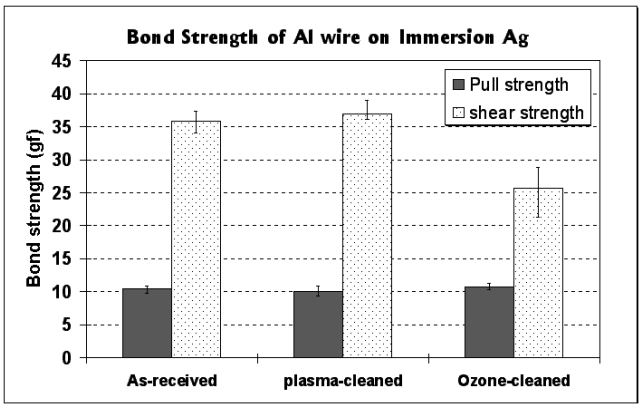

Fig 14 : Pull Strength & Shear strength of Al wire on as-received, plasma-cleaned and UV/Ozone-cleaned immersion Ag samples

Concluding Remarks

Immersion Ag has a lower metallization thickness, smaller grain size and finer surface morphology with lower roughness than immersion Sn. Both the coatings contain C and O throughout the layers indicating that the immersion Ag and immersion Sn finishes are not purely metallic but organometallic in property. This is intentionally made by the manufacturer in order to lower the material cost and improve the coating quality with less susceptibility to oxidation and growth of whisker [3,4,9,11]. Furthermore, a trace amount of S was detected at the Ag surface due to tarnishing. A trace amount of Cu was also detected due to the migration of underlying Cu substrate to the surface. Migration of Ag and Cu was also reported to occur across the bonded wire material with continuous composition change along the 1st and 2nd bonds [12].

Al and Au wires could be bonded to the immersion Ag surface. However, no wire could be bonded to the immersion Sn finish even after plasma or UV/Ozone cleaning. The surface roughness and thickness of Sn are much higher than Ag finish, but it appears that they are not crucial factors for a good bond to be formed. Instead, the nature of the metallization plays a more important role in intermetallic formation during the bonding process. A good bond can only be formed when the intermetallic compound is tough enough as a medium to glue the wire and the pad together. It is obvious that in our study, the Ag substrate formed a much stronger intermetallic compounds than the Sn substrate with either Al wire or Au wire.

To further explain why bonding can be produced on Ag surface, but not on Sn surface, wire bond is considered as a micro-welding process between two metals [13]. Not all, but selective metals, may be ultrasonically bonded through the formation of reliable intermetallic compounds. Based on the phase diagram for two-component metals, if intermetallic compounds exist and have high melting points of around 1000°C, bonding can be formed. If, however the intermetallic compounds have low melting points of less than 500°C, their constituents will continue to diffuse, good bonding cannot be formed. Compared between Ag and Sn, Ag has a melting point of 961 °C whereas Sn has 232 °C only. According to the phase diagrams of Al-Sn and Au-Sn systems [14], although the melting points of the corresponding intermetallic compounds are higher than pure Sn itself, they are mostly still below 500°C. This may be one of the reasons why bonding cannot be made on Sn finish with Al and Au wires.

Another possible cause for non-bondability of Sn finish is the large grain size and high hardness with brittle nature of the crystal at surface. With such well-defined polygonized crystallinity, bonding may be difficult to make with foreign wire materials. Previous study on Au metallization had also proved that hardness of substrate surface would affect wire bondability [8], but all these need further study to verify in the case of Sn finish.

When the bondability of Al and Au wires on the Ag finish is compared, the Al wire performed better than Au wire in terms of bond strength and its tolerance to surface oxidation and tarnishing.

Plasma cleaning of immersion Ag finish had slight improvement in bondability. However, UV/Ozone cleaning had an adverse effect on bondability due to the accelerated oxidation and tarnishing of the coating.

Contamination, whether organic or inorganic orgin like oxidation and tarnishing, is known to be detrimental for bondability [15,16,17]. As cleaning is not effective in removing oxidation and tarnishing to improve bondability in our case, it is therefore recommended to store the immersion Ag finished product in an air conditioned store room to prevent oxidation, rather than using various cleaning processes to remove contaminants afterwards.

Acknowledgements

The authors wish to thank the Research Grant Council (HKUST6014/98E) for financial support of this project. Characterization experiments were carried out with technical supports of Materials Characterization & Preparation Facility (MCPF) and Electronic Packaging Laboratory (EPACK) at HKUST. Bonding experiments were carried out at ASM Assembly Automation Ltd.

References

[1] Y.M. Cheung, S.W. Or and A. Sze, "*Revisit of Wirebonding on Immersion Silver-Finish Board"*, Int'l Symp on Electronic Materials & Packaging, 2000, pp.444-448.

[2] D. Hillman, B. Bratin and M. Pavlov, *"Wirebondability and Solderability of Various Metallic Finishes for Use in Printed Circuit Assembly"*, Surface Mount International Proc. Technical Program, Vol. II, 1996, pp. 687-701.

[3] D.H. Ormerod, *"Immersion Tin as a High Performance Solderable Finish for Fine Pitch PWBs"*, Circuit World, 26, 2000, pp.11-16.

[4] P.T. Vianco, *"An Overview of Surface Finishes and Their Role in Printed Circuit Board Solderability and Solder Joint Performance"*, Circuit World, 25, 1998, pp.6-24.
[5] S. Beigle, *"Non-precious Metal Coatings for Fine Pitch Assembly and Direct Chip Attachment"*, Surface Mount International, Proceeding Technical Program, Vol II, San Jose, 1996, pp.780-785.
[6] C. Hutchinson, "Training & Information Manual for Alpha Level Line", Training Material, AlphaMetal. 1999.
[7] D.H. Ormerod, *"Production Application of Flat Solderable Tin Finishes -- Some Practical Considerations"*, Datasheet from Polyclad Technologies. 2000.
[8] J.K. Kim and B.P.L. Au, *"Effects of Metallization Characteristics on Gold Wire Bondability of Organic Printed Circuit Boards"*, Journal of Electronic Materials, Vol.30, 2001, pp.1001-1011.
[9] T. Kakeshita, K. Shimizu, R. Kawanaka and T. Hasegawa, *"Grain Size Effect of Electro-plated Tin Coatings on Whisker Growth"*, Journal of Materials Science, 12, 1982, pp.2560-2566.
[10] Y. Itoh, H. Haji, H. Nakashima and H. Kishida, *"Ultramicrotomy of Wire-bonded Interfaces for TEM Observation"*, Electron Microsc, vol. 44, 1995, pp.151-152.
[11] B. Wessing, *"Use of Organic Metal to Enhance the Operating Window and Solderability of Immersion Tin"*, Circuit World, 25, 1998, pp.8-16.
[12] K.C. Hsieh and T. Martens, *"Ag and Cu Migration Phenomena on Wire Bonding"*, Journal of Electronic Materials, Vol.29, 2000, pp.1229-1232.
[13] G.G. Harman, *"Wire Bonding in Microelectronics Materials, Processes, Reliability AND Yield"*, 2nd edition, McGraw-Hill, New York, 1997, pp.6-10.
[14] J.H. Westbrook, *"Handbook of Binary Phase Diagrams"*, Genium Publishing Corporation, Vol. 1, August, 1997.
[15] A. Schneuwly, P. Groning, L. Schlapbach and V.P. Jaecklin, *"Influence of Surface Contamination on Metal/Metal Bond Contact Quality"*, Journal of Electronic Materials, Vol.27, 1998, pp.990-997.
[16] F. Fazlin, *"Plasma Treatment for Improved Wire Bonding",* Solid State Technology, vol.39, Oct. 1996, pp.117-120.
[17] G.G. Harman, *"Wire Bonding in Microelectronics Materials, Processes, Reliability AND Yield"*, 2nd edition, McGraw-Hill, New York, 1997, pp.142-147.

The Behavior of FAB (Free Air Ball) and HAZ (Heat Affected Zone) in Fine Gold Wire

Sung-Jae Hong, Jong-Soo Cho, Jeong-Tak Moon, and Jin Lee
R&D, MK Electron Co. LTD
Yong-In, Korea, 449-810
E-mail) sjhong@mke.co.kr, Tel) +1-82-31-330-1942

Abstract

The trend of high integration and miniaturization of semiconductor has accelerated the development of gold bonding wire with smaller diameter. For the stable bonding of fine wire, it is important to characterize the wire with various diameters during the bonding process. To investigate this relationship, the experiments were done for the various sizes of wire diameter and FAB. The wire size and the FAB size were chosen for the test from 15 um to 25 um and from 1.4 WD (Wire Diameter) to 2.0 WD, respectively. The results showed that as the size of FAB became smaller, the size deviation of FAB increased and FAB itself was tilted to one side. When FAB was formed at the same parameter, the length of HAZ became shorter for the wire with the high temperature of recrystallization. It is also revealed that the length of HAZ decreased for the smaller size of FAB. This phenomenon is considered to be related to the heat generated during the FAB formation.

Introduction

Rapid advance of information and technology industry requests high performance, miniaturization and portability of semiconductor products. For the reason, the size of Si chip (Die) is decreased and highly integrated. To integrate more I/O on the reduced Si-Die, the gap of BPP (Bond Pad pitch) and the size of BPO (Bond Pad Open) should be narrower and smaller, respectively. Currently, the 50 μm BPP Mass Product is produced using 0.8 *mil* wire in the assembly process, and the diameter of wire will become smaller and smaller, as shown in Figure 1.

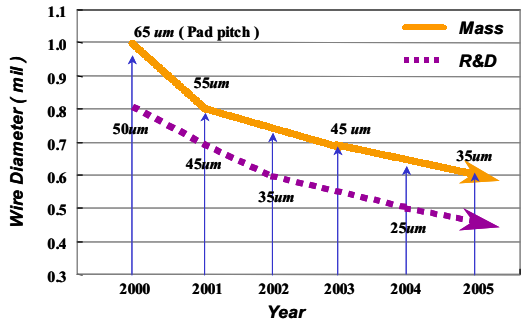

Figure 1. The trend of wire size with respect to the variation of Bond Pad Pitch.

As the wire size becomes smaller, there occur many problems such as low breaking load, high electrical resistance, instability of bonding loop, serious mold sweeping, etc. Since the size deviation and the miss control of Free Air Ball are directly related to the defect modes of wire bonding such as off-centered bond and ball-lift, the Free Air Ball Control of fine wire is considered to be very critical for the decreased BPP and BPO. [1-3] Also, the thinning of PKG causes to lower the bonding height which depends on HAZ variation. Therefore, many researches are focused on decreasing the length of HAZ because the length of HAZ has the direct relationship with the ball neck damage of loop height control.

In this research, the wire properties, the FAB (Free Air Ball) size deviation, and the ball shape variation due to the wire size reduction were investigated. Also, the wire bonding problems for the decreased wire diameter were predicted by observing HAZ variation at each condition, [4]

Experiments

Wire Fabrication

The wires used in this experiment were fabricated in the production line of MK Electron Co. Dopant was added to 5N gold, and then the ingot is made by continuous casting process. Two kinds of wires were made according to *Ca* content: normal wire and hard wire. The wires were fabricated by the drawing process of the reduction ratio of 12-7%, and became the fine wires of 1.2 *mil* – 0.6 *mil* (30 μm-15 μm). Then, internal stress and wire curl were removed through the annealing process.

Measurement of Mechanical and Electrical Properties

B/L (Breaking Load) and E/L(Elongation) of the wires were measured at 20°C(Room Temp.) and 250°C(High Temp.) using *AND RTC 1150A* tensile tester with the cross head speed of 10 *mm*/*min* and the gauge length of 100 *mm*. Electric resistance was observed using Micro-Ohm Meter, *HP34420A*, with the measuring length of 300 *mm* and 4 point probe method.

Measurement of Free Air Ball (FAB) Formation and Its Size

Free air ball was made from 0.6, 0.7, 0.8, and 1.0*mil* wires using the automatic wire bonder. The size of FAB at each wire size was measured for various EFO (Electronic Flame Off) Parameters. The accuracy of the EFO Current Level was ± 0.1 *mA*, and the resolution of the EFO time was ± 0.001 *ms* according to the specification of the EFO generation system. Measurement of ball sizes was done using Hisomet, a measurement microscope with 500 times magnification. The resolution of measurement was ± 0.1 μm. The fabricated FAB was observed by SEM (Scanning Electron Microscope) to

investigate off-centered degree. The configuration of off-centered degree is helpful to predict that the off-centered bond occurs as the wire becomes thinner.

Variation of HAZ (Heat Affected Zone)

HAZ lengths were observed for each wire size using FAB with 2 times larger than wire diameter. HAZ lengths were also measured for 1.0 *mil* (25 μm) wire diameter by decreasing the wire size of FAB from 2.0 times to 1.4 times step by step.

HAZ was investigated by etching FAB using aqua-regia, taking SEM image, and observing grain size. Then, HAZ was determined as the distance between the ball part and the position which shows the original grain size. (See Figure 2)

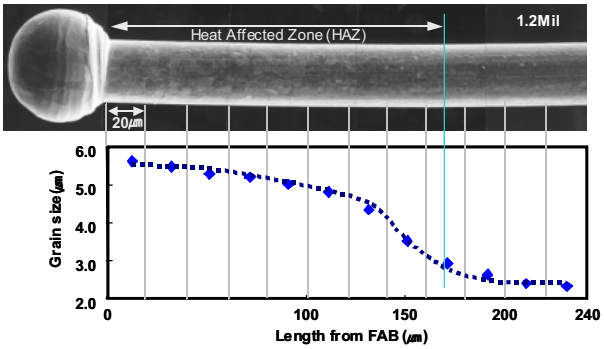

Figure 2. The method to measure HAZ in MKE.

Results

Wire Properties with respect to Wire Size

B/L(Breaking Load) of Normal wire (Ca = 5 ppm, others 40 ppm) and Hard wire (Ca = 30 ppm, others 40 ppm) which have different amount of Dopant is shown in Figure 3. Hard wire shows about 20 % higher mechanical property than that of 4 N Normal gold wire at room temperature and high temperature. When Ca is added as a Dopant, strong stress field is formed around Ca because the atomic radius of Ca is larger than that of gold. (Au = 1.44 *nm*, Ca = 1.97 *nm*) This disparity causes the stress field and B/L increases. The increased B/L results in the better mechanical property of wire.

B/L of hard wire at high temperature decreased less than that at room temperature. The B/L ratio of high temperature to room temperature was 0.91(hard wire) and 0.88(normal wire) respectively. The hard wire with more Ca amount shows the higher B/L at high temperature, because Ca has higher specific heat than Au (Au = 130 *J/KgK*, Ca = 624 *J/KgK*). The difference of B/L between hard wire and normal wire was 2.0 *gr* for 1.0 *mil* diameter, whereas it was 0.5 *gr* for 0.6 *mil* diameter.

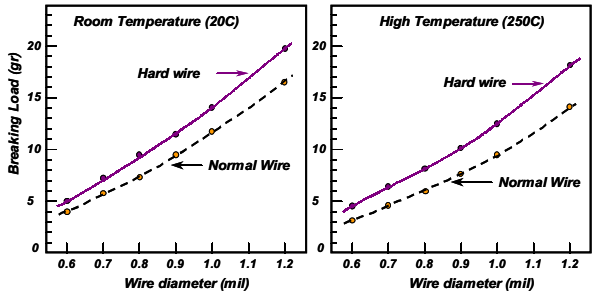

Figure 3. Breaking load change against wire size.

Figure 4 shows the electric resistance and the fusing current change with wire size. Electric resistance, *R*, was proportional to $4L/\pi D^2$ and the resistance increased abruptly as the wire diameter was smaller.

The fusing current also reduced, as the wire size decreased. For example, the melting current of 1.0 *mil* gold wire with 5 *mm* wire length was 0.56 *A*, and, for 0.6 *mil* diameter, the current was 0.2 *A*. The fusing current was calculated by the following theoretical equation. [5]

$$I_f = d^2 \times 10^2 \sqrt{(2.948 \times t_f^{-1}) + (1.884 \times 10^3 \times l^2)}$$

where I_f (*A*), t_f (*s*), *d* (*mm*), and *l* (*mm*) are fusing current, fusing time, wire diameter, and wire length, respectively. Consequently, the reduction of the wire size causes the deterioration of electrical performance.

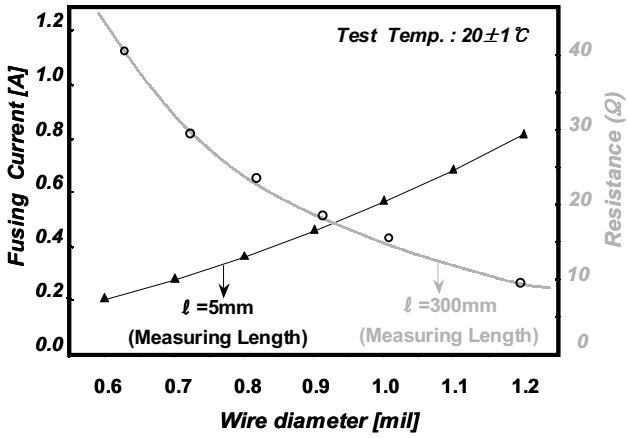

Figure 4. Electric resistance and fusing current against wire size.

FAB Size Due to the Decrease of Wire Size

Figure 5 shows the average and standard deviation of FAB size which was made of 2 times larger diameter of the wire by controlling EFO parameter. As FAB size decreased from 1.0 *mil* to 0.6 *mil*, the deviation of FAB size increased from 1.0 to 2.3, Finally, the thinner was the wire size, the larger was the standard deviation of FAB size.

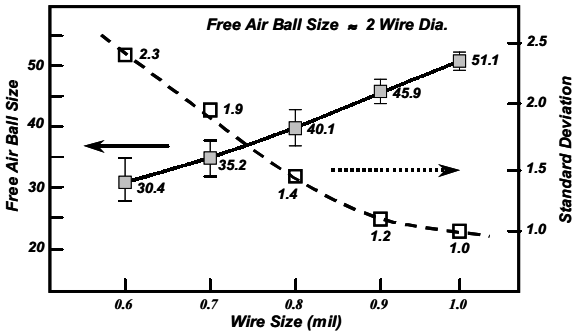

Figure 5. FAB size deviation against wire size.

FAB Shape Due to Decrease of Wire Size and FAB Size

Figure 6 shows the off-centered (X1/X2) degree which indicates the tilt of FAB from the center of wire, when the wire size and the FAB size are changed. [6] It is revealed that the degree of asymmetry increases, as the wire diameter becomes thinner and the FAB size decreases.

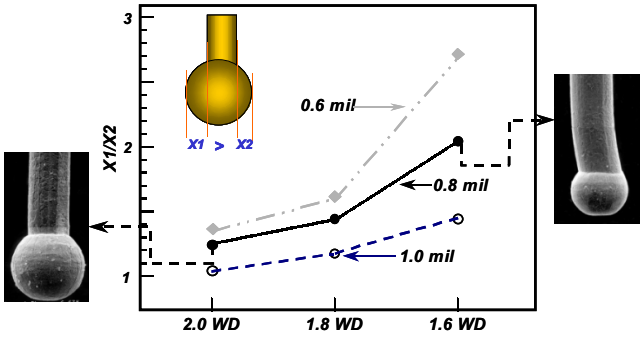

Figure 6. FAB shape deviation against wire size & FAB size.

Figure 7 explains why the asymmetry increases as FAB size decreases. The capillary pushes down and breaks off the wire (A) during the stitch bond (2nd Bond) process, and then the tail end of the wire is bent after the stitch bonding. At this condition, FAB is formed by applying EFO at the end of wire to do 1st Ball Bonding. If the size of FAB is small, the bent part is not completely melted. Thus, the formed Ball becomes asymmetry (C-1). If FAB size is large enough to melt the bent part of the tail, FAB becomes symmetry.

From the above results, FAB formation gets unstable, as wire size is fine. Thereby, the probability of small ball or off-centered bond increases in 1st bond. In order to form the stable 1st bond, the size deviation and the asymmetry of FAB should be reduced. The small capillary hole and chamfer diameter, the improvement of tail shape by optimizing 2nd bond parameter, and the higher accuracy of EFO current and time by improving EFO generator are recommended to reduce the deviation and the asymmetry.

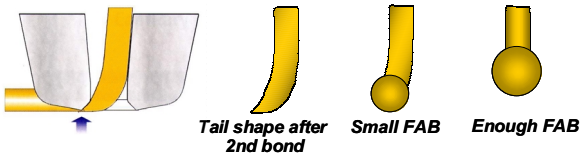

Figure 7. Tail shape after 2nd bond and ball formation.

Heat Affected Zone (HAZ) Length Due to Wire Size and FAB Size

Figure 8 shows HAZ length variation due to the change of FAB size with same diameter. As FAB size was smaller, HAZ length decreased. In the ball bonding process, the wire is melted by EFO to form FAB, and some part of wire is exposed to heat which is needed to form FAB. This zone has greater grain size than that of other wire parts and it is called Heat Affected Zone (HAZ). For the small FAB, the heat energy is less relatively and thus the HAZ length decreases.

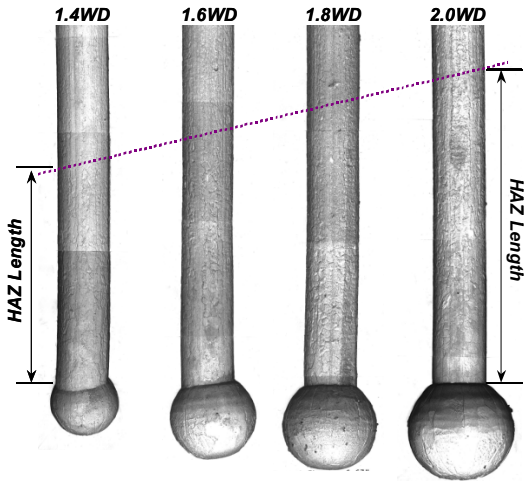

Figure 8. HAZ variation against FAB size.

The HAZ variation was shown in Figure 9 against FAB size when FAB was 2 times larger than wire diameter. The heat-transferring section area of wire and the volume of FAB are proportional to the square and the cube of wire diameter, respectively. In order to form FAB with the constant ratio of wire diameter, the corresponding heat should be applied. Thus, the thinner is the wire, the shorter is the HAZ length. Since the hard wire includes more Ca-dopants and increases activation energy highly for grain growth to make the shorter HAZ length, HAZ of hard wire was shorter than that of normal wire for the wires of same diameter.

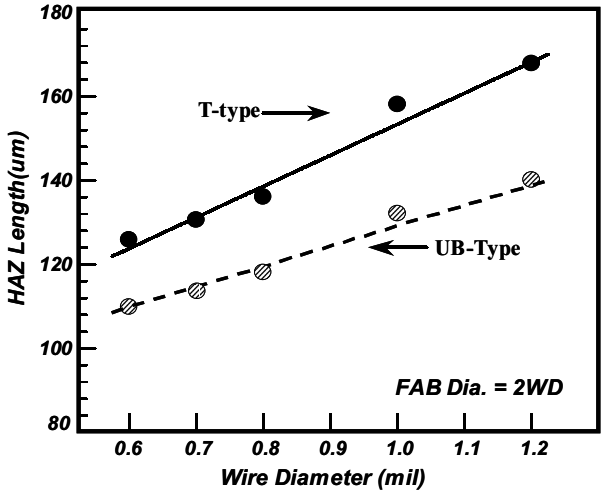

Fig. 9 HAZ length variation against wire size.

Conclusions

Two kinds of wires fabricated by changing *Ca* dopant content showed that there is 20 % difference in Breaking Load values. Conclusions obtained from the results of FAB ball size deviation and HAZ length are follows.

As FAB size became smaller, the size deviation of FAB increased. When wire diameter was thinner, FAB size is smaller, the deviation of FAB shape increased. The length of HAZ became shorter for the wire with the high temperature of recrystallization, as FAB was formed at the same parameter. It was also revealed that the length of HAZ decreased as the smaller size of FAB.

References

1. George G. Harman, "Wire Bonding in Microelectonics", McGraw-Hill Book Company, 2nd Edition, 1997.
2. Texas Engineering Extension Service, "Wire Bond", TEEX, Feb. 1998.
3. Zeno Stoessel, "Pushing the Limits of Ultra fine Pitch bonding with a Ball Deformation Analysis," Semiconductor Packaging Symposium in San Jose on 15, July.
4. Wei(Ivy) Qin and Ira M. Cohen, "Ball Size and HAZ as Functions of EFO Parameters for Gold Bonding Wire", EEP-Vol. 19-1, Advanced in Electronic Packaging – 1997, Vol. 1, ASME, pp391-398.
5. Atila Mertol Member, "Estimation of Aluminum and Gold Bond Wire Fusing Current and Fusing Time", IEEE, Tranc-CPMT-B, Vol.18, No 1 (Feb. 1995).
6. Jun-Ichi Oikawa, "Gold Wire Enhanced Thermo-compression, Thermosonic Wire Bonding", Journal of Electronic Engineering 32(343), July 1995, pp.22-30.

Effects of Cu/Al intermetallic compound (IMC) on copper wire and aluminum pad bondability

H. J. Kim*, J. Y. Lee*, K. W. Paik*, K. W. Koh**, J. H. Won**,
S. H. Choi**, J. Lee***, J. T. Moon*** and Y. J. Park***
*MicroElectronic Packaging Lab.(MEPL), Department of Materials Science and Engineering , KAIST
373-1, Kusung-dong, Yusung-gu, Taejon 305-701, Korea
Phone : +82-42-869-3375, e-mail : semimat@mail.kaist.ac.kr
**ASE Korea, 494, Munbal-ri, Kyoha-myun, Paju-si, Kyunggi-do, 413-830, Korea
***MK Electronics, 316-2, Kumeu-ri, Pogok-myun, Yongin-si, Kyunggi-do, 449-810, Korea

Abstract

Copper wire bonding is an alternative interconnection technology to serve as a viable, and cost saving alternative to gold wire bonding. Its excellent mechanical and electrical characteristics attract the high-speed, power management devices and fine-pitch applications. The copper wire bonding will be an important interconnection technology along with a flip chip technology.

However, the growth of Cu/Al IMC (intermetallic compound) at the copper wire and aluminum interface can induce a mechanical failure and increase a potential contact resistance. In this study, the copper wire bonded chip samples were annealed at the temperature range from 150°C to 300°C for 2 to 250 hours, respectively. The formation of Cu/Al IMC was observed and the activation energy of Cu/Al IMC growth was obtained from an Arrhenius plot (ln (growth rate) vs. 1/T). The obtained activation energy was 26Kcal/mol. And the behavior of IMC growth was very sensitive to the annealing temperature.

To investigate the effects of IMC formation on the copper wire bondability on Al pad, ball shear tests were performed on annealed samples. For as-bonded samples, ball shear strength ranged about 240 ~ 260 gf, and ball shear strength changed as a function of annealing times. For annealed samples, fracture mode changed from adhesive failure at Cu/Al interface to IMC layer or Cu wire itself. The IMC growth and the diffusion rate of aluminum and copper closely related to failure mode changes. Micro-XRD was performed on fractured pads and balls to investigate a major forming IMCs and their effects on the ball bonding strength. From XRD results, it was confirmed that the major IMC was γ-Cu_9Al_4 and it provided a strong bondability.

1. Introduction

There are several chip interconnection techniques such as wire bonding, TAB (Tape Automated Bonding), and flip chip technology. Wire bonding has been used for its advantage of better-stability and cost effectiveness over other chip interconnection techniques despite the current trend to flip chip interconnection. Wire bonding is still regarded as one of the most important cost effective chip interconnection technologies even though flip chip technology has been highlighted on the use of high I/Os and high-speed devices.

For bonding wires, gold and aluminum have been commonly used. Recently, instead of Al-metallization used in semiconductor industry, Cu-metallization and interconnection technology have received much attention due to its better electrical performances in comparison with aluminum. Therefore, many studies on the copper wire bonding are being in progress [1-4]. There are several disadvantages and advantages. The disadvantages of copper wire are as follows :

First, the technology of copper wire bonding is not well convinced in the industry because additional bonding parameters such as the forming gas need to be defined and optimized. Second, due to the easy oxidation of copper, copper wire bonder requires special tools to prevent copper oxidation. Copper wires need higher energy than gold wires when they are bonded to pads. However, copper wires also provide many advantages that are superior to gold wires. The advantages of copper wires are as follows :

First, copper wire is 3 to 10 times lower in cost compared to gold wire. Second, copper wire shows superior mechanical and electrical properties to gold and aluminum wires. Excellent electrical conductivity and small amount of heat generation allow copper wire to be use not only for power management devices but also for thinner diameter wires to accommodate small pad sizes. The high rigidity of copper wires is considered more compatible to the fine pitch bonding than gold wires. Third, slower intermetallic compound (IMC) growth between copper wires and aluminum pads results in lower contact electrical resistance and better reliability in comparison to gold wires and aluminum pads. Making electrically and mechanically stable mono-metallic bonding interface, copper wires to copper pads system at the high-speed chip, is the final goal of using copper wires in. Copper to copper mono-metallic interface does not form brittle IMC phases, so it is expected to eliminate mechanical problems and to maintain stable electrical properties due to no IMC formation. Copper pad technology as an alternative pad system has not yet been accepted in the industry practically, because copper is easily oxidized and its oxidation layer acts as an obstacle to the bonding process. This is why the established aluminum pad has been used in this study instead of the copper pad.

Cu-Al IMC phases

One of the most serious factors making a failure between gold wire and aluminum pad is the IMC formation, called “purple plague”. Many researchers have established theories on the IMC formation of Au/Al system and its effects on the bondability [5-6]. In the case of Cu/Al system, some studies on IMC formation during annealing were reported using welded diffusion couple of bulky copper and aluminum [7-8] or thin film Cu/Al diffusion couple [9-10]. However, it was found difficult to observe IMC formation in practical copper wire to aluminum pad bonding. Generally, the IMC formation in Cu/Al system is much slow compared to the Au/Al system.

Therefore, copper wires on aluminum pads show higher mechanical reliability and smaller increase in the electrical resistance than that of gold wires on aluminum pads.

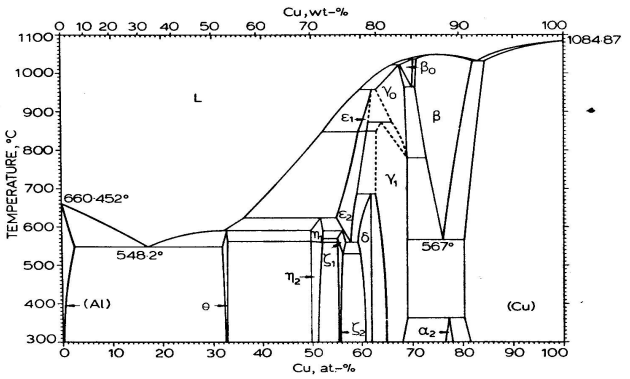

Fig. 1. Phase diagram of Cu-Al system.

The phase diagram of Cu-Al system shown in Fig. 1 identifies the possible IMCs formed between copper and aluminum. Cu/Al IMC phases which formed at the temperature range between 150°C to 300°C are as follows [7] :

γ_2 phase (Cu_9Al_4) : 69.2 atm% Cu
δ phase (Cu_3Al_2) : 60.0 atm% Cu
ζ_2 phase (Cu_4Al_3) : 57.1 atm% Cu
η_2 phase (CuAl) : 50.0 atm% Cu
θ phase ($CuAl_2$) : 33.3 atm% Cu

During packaging processing and chip operation, temperature can reach to interdiffusion of copper and aluminum at the bonding interface. The diffusion rate of aluminum into copper is faster than that of copper into aluminum. Therefore, Cu/Al IMCs grow at the bonding interface. Generally, significant IMC growth can make the bonding interface brittle and acts as a major cause for bonding failure. However, moderate IMC growth increases the bonding strength by alloying between copper and aluminum.

In this study, we investigated the effects of IMC growth on the bondability of copper wire and aluminum pad.

2. Experiments

The bonding parameters of copper wire

The copper wire was bonded to the Al/1%Si/0.5%Cu pad of 2μm thickness using the Shinkawa CUB-300BI machine. Table 1 and Table 2 show the properties of a copper wire and bonding parameters for making samples.

Table 1. Properties of a copper wire

Composition	Cu (99.996%)
Diameter	2.0 mil
Specified Breaking Load (g)	40 ~ 45
Average Breaking Load (g)	47.5
Specified Elongation (%)	15 ~ 25
Average Elongation (%)	19.7

Table 2. Wire bonding parameters

Bonding Time (ms)	30
Bonding Load (mN)	160
Ultrasonic Power (mW)	160

Specimen preparation

Annealing was performed in the convection oven at 150°C, 250°C, and 300°C (controlled within ±5°C) for 2 hours up to 250 hours, respectively. During the annealing, nitrogen gas was purged into the convection oven continuously to prevent the copper oxidation, because copper can be easily oxidized at these high temperatures.

IMC growth evaluation

IMCs are different from copper and aluminum in colors. The presence of IMC can be checked using colors change under on optical microscope (OM). And a SEM, as a supplementary experiment, was also used to identify IMCs. DI water and HNO_3 mixed solution was used to etch copper selectively. IMC thickness, which grew as functions of annealing temperatures and times, was measured by OM and SEM. The least square method was employed for obtaining the reaction rate of Cu/Al IMC formation. Theoretical thickness of Cu/Al IMC by applying the obtained reaction rate was calculated, and compared with the observed thickness. Finally, bonding stability can be confirmed through the comparison of the obtained reaction rate of Cu/Al IMC with that of Au/Al IMC.

Ball shear test (Fracture analysis)

Ball shear test is a kind of destructive test that measures the energy involved in the fracture of ball bonding. Tests were performed on annealed copper wire samples bonded on the aluminum pads to investigate the effects of IMC formation on copper wire bondability.

The ball bond shear data presented in this study were obtained using Dage series 4000, and the test conditions were as follows:

Ball shear height : 4 μm from chip surface
Stylus moving speed : 300 μm /s
Overtravel length : 100 μm

More than 30 wires were sheared in each condition in order that test results would satisfy a standard normal distribution. To investigate the failure mode at bonding interface, the fractured pads and balls were observed using OM and SEM.

Micro-XRD

Micro-XRD experiment was performed on the fractured pads and balls after the ball shear test to understand the effects of Cu/Al IMC formation at the interface. The identification of IMC phases was done by matching the micro-XRD results to the JCPDS card, and the obtained results of phase identification were compared with that of EDS.

The micro-XRD uses a fine collimator with 50μm diameter to test on a small-swized specimen. It took a long time to have the XRD patterns because the X-ray beams were scattered inside the collimator resulting in weak intensity. The

obtained diffraction patterns showed some differences from the diffraction patterns of powder samples, but identifying the IMC phases was not difficult.

3. Results and Discussion

3.1. Cu/Al IMC observation

Fig. 2 shows the cross-sectional images of Cu/Al IMC which formed at the bonding interface. It was difficult to find out the formation of IMC in OM images at 150°C for 25 hours. However, light-colored images can be observed at the Cu/Al interface in SEM images. In case of 250°C of annealing, light-colored images appeared at 150°C, 50 hours-annealed samples were quickly observed even in the 2 hours-annealed samples at 250°C. IMC thickness grew about 0.5 μm after 25 hours of annealing at 250°C. After 100 hours of annealing, very clear IMC layer was formed at the Cu/Al interface because of significant growth of Cu/Al IMC at the bonding interface after annealing at high temperatures for a long time. Color of IMC layer was yellowish in OM images.

At 300°C, the yellowish IMC layer was clearly observed even after 5 hours of short annealing, and the bluish aluminum pad was completely disappeared after 100hours. Aluminum was consumed very fast due to the rapid diffusion into the copper wire, and the high reaction rate of the formation of Cu/Al IMC at high annealing temperatures.

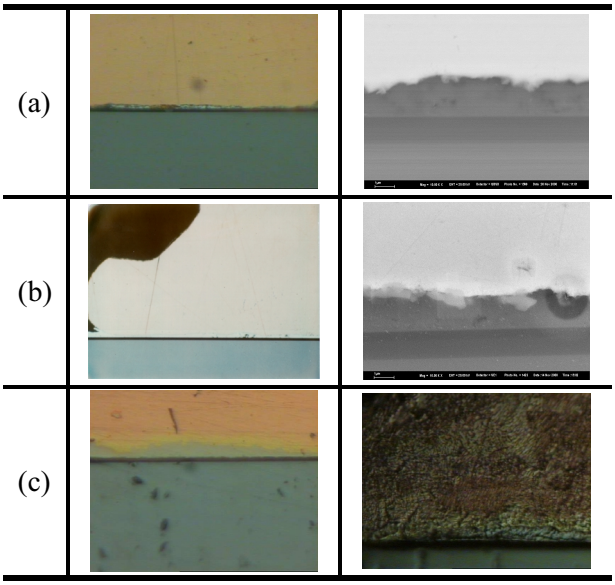

Fig. 2. Cross-sectional images of OM and SEM of Cu/Al interface after annealing treatment at (a) 150°C, 25 hours, (b) 250°C, 25 hours and (c) 300°C, 25 hours.

EDS analysis was performed to investigate the composition ratio of each element at the yellowish IMC layer observed at annealed samples. Fig. 3 shows the cross-sectional SEM image of 100 hours-annealed specimen at 250°C, and the layers are distinguished as the change of colors. EDS was carried out at A, B, and C points, and results are shown in Table 3. According to results shown in Table 3, Al rich phase was formed at the A point, close to aluminum pad, and Cu rich phase at C point, close to copper wire. Table 3 indicates that several different IMC phases can be formed at the bonding interface. In the case of a welded bulk Cu/Al diffusion couple, many former researchers reported that all possible IMC phases such as $CuAl_2$ (θ), CuAl (η_2), Cu_4Al_3 (ζ_2), Cu_3Al_2 (δ), and Cu_9Al_4 (γ_2) are formed layer by layer [7] from aluminum to copper. In the diffusion couple of thin film type, the reported IMC phases were $CuAl_2$, CuAl, and Cu_9Al_4 [9-10], but many researchers had difficulty in distinguishing IMC layers clearly. Several variables such as the shape of specimen, annealing temperature, and time can affect the formation and the growth of IMC, and thereby change the possible IMC phases. In our experiment, it was also difficult to distinguish all IMC phases layer by layer.

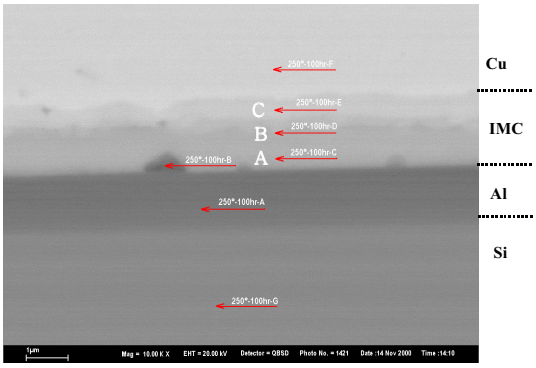

Fig. 3. SEM image of annealed Cu/Al sample at 250°C for 100hr. EDS analysis was performed at A, B, and C points.

Table 3. The result of EDS analysis on the sample annealed at 250°C for 100 hr.

	A point	B point	C point
Al (atm%)	34.97	59.08	55.29
Cu (atm%)	14.28	24.23	40.68
Si (atm%)	50.75	16.69	4.03
Cu:Al ratio	~ 1:2	~ 1:2	~ 1:1

3.2. The growth behavior of Cu/Al IMC

The growth rate of Cu/Al IMC was determined by measuring the thickness of the inter-diffusion layers after annealing. Fig. 4.(a) shows the parabolic growth behavior of IMC. At early stage of annealing, IMC thickness grew fast. However as annealing times increased, the IMC growth rate decreased. Moreover, the IMC growth significantly depend on annealing temperature. Fig. 4.(b) shows IMC thickness versus $(\text{annealing time})^{1/2}$ to confirm whether IMC growth follows a parabolic law. The IMC growth follows the parabolic law, although there were slight deviations at 300°C annealing presumably due to the rapid IMC growth at the early stage. The reaction rate of IMC formation shown in Table 4, K, can be obtained from Fig.4.(b).

Within the experimental data, the relationship between the IMC thickness (X) and the annealing time (t) at a given temperature can be represented by

$X^2 = K\,t$ X = IMC thickness (μm)

t = annealing time (s)

K = Reaction rate of IMC formation (cm^2/s)

where K is characterized by the temperature and the activation energy. So it is given as

$K = K_0 \exp(-\Delta Q/RT)$ Q = Activation energy (kcal/mol)

R = Gas constant

T = Annealing temperature (^oK)

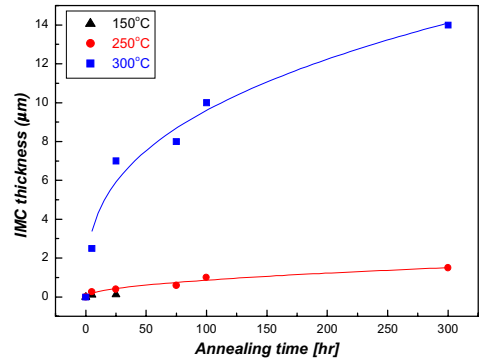

(a)

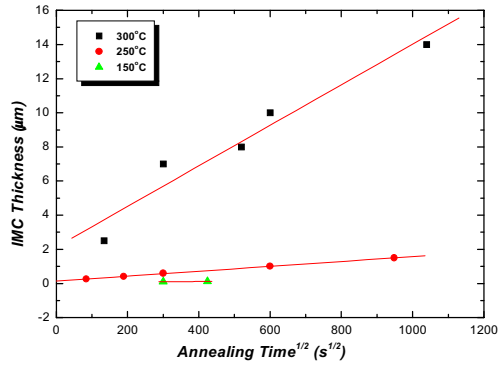

(b)

Fig. 4. (a) IMC thickness versus annealing time (hr). (b) IMC thickness versus annealing time$^{1/2}$.

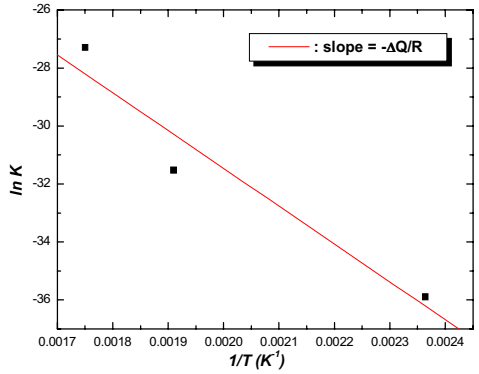

Fig. 5. Logarithm of the reaction rate in Cu/Al IMC formation as a function of inverse temperature.

Table 4. The reaction rate of Cu/Al IMC growth at various temperatures.

Temperature(^{o}C)	K, Reaction rate (cm^2/s)
150	1.878×10^{-16}
250	6.833×10^{-14}
300	6.027×10^{-13}

Table 5. Comparison of the reaction rate of Au/Al IMC formation with that of Cu/Al IMC formation.

Temperature (^{o}C)	Au/Al, K (cm^2/s)	Cu/Al, K (cm^2/s)
150	1.1×10^{-14}	1.878×10^{-16}
280	2.4×10^{-11}	2.645×10^{-13}
350	3.9×10^{-10}	3.747×10^{-12}

and the reaction rate constant K and the activation energy Δ Q can be calculated from ln K versus 1/T curve shown in Fig. 5. The obtained activation energy was about 26 Kcal/mol, but this was slightly different from the reported activation energy, 29 ~ 34 Kcal/mol, obtained from the bulk Cu/Al diffusion couple [7-8].

As a result, the IMC growth can be explained by annealing temperature (T) and time (t) :

Derived IMC growth equation :

$X^2 = t\ 4.658X10^{-3} \exp(-13046.17947/T)$

Theoretical thickness of IMC formation can be calculated by this expression.

Table 5 shows that the comparison of calculated reaction rates of Cu/Al IMC formation and that of Au/Al IMC formation. At certain temperature, the reaction rate of Cu/Al IMC is 100 times slower than that of Au/Al IMC. The IMC thickness is proportional to the square root of K so that the thickness of Cu/Al IMC is expected 10 times thinner than that of Au/Al IMC at the same annealing condition. Kirkendall voids, formed at gold wires on Al pads, were not observed at copper wire bonding interface. Consequently, the copper wire bonding can provide better mechanical and electrical reliability because of the slow growth rate of Cu/Al IMC and the absence of the Kirkendall voids.

3.3. Ball shear test and failure mode analysis

Fig. 6. shows results of ball shear test of annealed samples at 150^{o}C, 250^{o}C, and 300^{o}C. Ball shear strength increased gradually as annealing time increases in cases of 150^{o}C and 300^{o}C of annealing. However, ball shear strength decreased as the annealing time increased at 250^{o}C. Failure analysis was performed to analyze the changes of ball shear strength. Fig. 7. shows the OM and SEM images of fractured pads. Failure modes were different at each annealing temperatures. Types of failure mode were divided into Mode A, B, and Cdepending on annealing conditions.

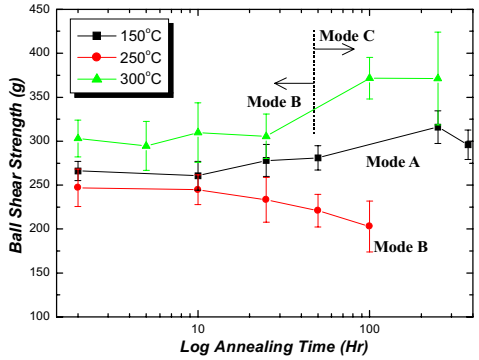

Fig. 6. Ball shear strength versus logarithm of annealing time at 150^{o}C, 250^{o}C, and 300^{o}C annealing temperature.

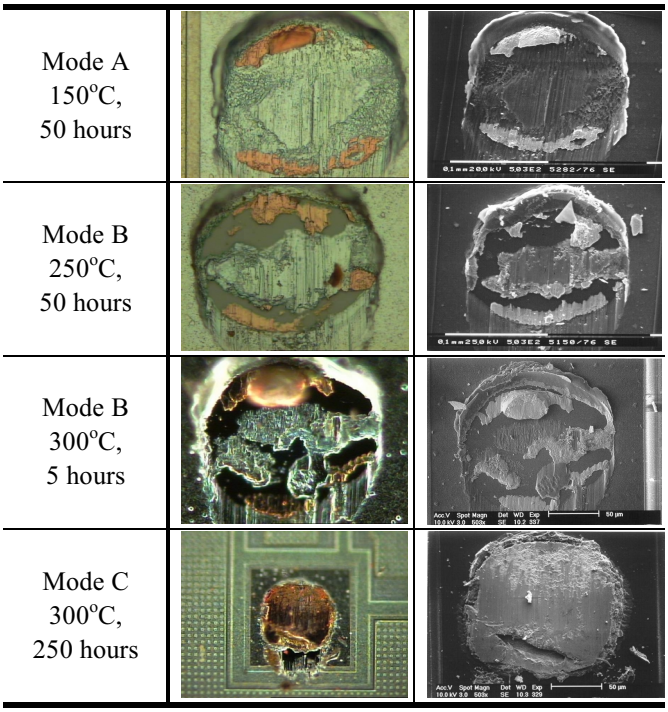

Fig. 7. OM and SEM images of fractured pads of annealed samples. Different failure modes were observed at each annealing conditions such as an adhesive interface failure (Mode A), the poor wetting failure (Mode B), and the cohesive failure inside Cu ball (ModeC).

150°C Annealing

Silver-colored area in OM images was known as aluminum by EDS analysis. Al pad occupied the major portion of fractured pads. The amount of remaining copper wire at the edge of the fractured pad increased gradually as annealing time increased. It is considered that the effect of Cu/Al IMC during the ball shear test was very minimal because Cu/Al IMC formation was difficult at 150°C. Therefore, fractures occurred at interface between copper wires and aluminum pads. The scratched marks of aluminum pads supported this Fig. 7. OM and SEM images of fractured pads of annealed samples. Different failure modes were observed at each annealing conditions such as an adhesive interface failure (Mode A), the poor wetting failure (Mode B), and the cohesive failure inside Cu ball (Mode C).

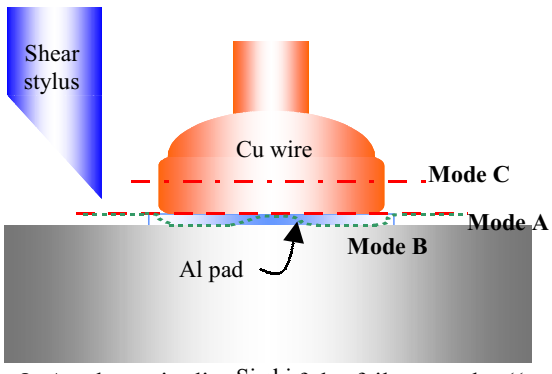

Fig. 8. A schematic diagram of the failure mode. ((- - -) Mode A; (·····) Mode B, and (- · -) Mode C)

analysis. The failure mode of 150°C was 'adhesive interface failure' (Mode A) and a schematic diagram of the Mode A failure is shown in Fig. 8. During longer annealing times, more copper and aluminum reacted resulting in a stronger interface. As a result, more copper was observed at the fracture pad at longer annealing time.

250°C Annealing

The images of fractured site annealed at 250°C are different from those at 150°C. Scratched aluminum pad, covered most area of the fractured sites at 150°C, remarkably disappeared, and the proportion of exposed SiO_2 below aluminum pads increased at 250°C. As annealing times increased, the area of SiO_2 increased and occupied about 50% of fractured sites after 100 hours annealing.

Due to the small quantity of the aluminum pad compared with the copper wire and the high diffusivity and reaction rate between copper and aluminum at 250°C, only 2 μm thickness of aluminum pad can be easily consumed during longer annealing time at 250°C. If aluminum was consumed entirely, Cu or Cu-rich IMC phase can meet SiO_2 layer underneath. The adhesion of Cu or Cu-rich IMC to SiO_2 may be weak resulting in a delamination at this interface during a ball shear test. The increase of exposed SiO_2 area indicates that most aluminum was consumed by the Cu/Al IMC reaction, thereby the portion of Cu-rich IMC/SiO_2 interface increased. The change of fracture site from Cu/Al adhesive interface to Cu/Al IMC/SiO_2 interface and low ball shear strength can be possibly explained by poor adhesion of Cu/Al IMC/SiO_2 interface. Conclusively, at 250°C the major failure mode is the Cu/Al IMC/SiO_2 interface (Mode B, shown in Fig. 8) and the adhesive interface failure (Mode A) is observed as a minor failure mode.

300°C Annealing

At 300°C annealing, until 25hours, fracture images were very similar to those of 250°C composed of scratched aluminum pads, remained copper wires and exposed SiO_2. After 100hours of annealed samples, ball fracture took place inside balls (Mode C). SiO_2 was not exposed after 250 hours. As shown in Fig. 6, the fracture mode changed from the Mode B to the Mode C after 25 hours.

The shape of fractured sites up to 25 hours (Mode B) was similar to those of 250°C of annealing, as shown in Table 6, because theoretical thicknesses of annealed samples at 250°C for 250 hours and at 300°C for 25 hours were almost identical based upon a simple calculation using reaction rate at 250°C and 300°C. Therefore, it is understood that identical IMC thickness of about 2.3 μm results in the similar fracture mode at different temperature.

Table 6. Theoretical IMC thickness after annealing (a) at 250°C and (b) at 300°C

(a) 250°C Annealing

Annealing time (hours)	IMC thickness (μm)
2	0.22
10	0.49

25	0.78
100	1.55
250	***2.48***

(b) 300°C Annealing

Annealing time (hours)	IMC thickness (μm)
5	1.00
25	***2.30***
75	4.00
100	4.65
250	7.36

After 25 hours of annealing at 300°C, the fracture site moved to inside the ball (Mode C) and the shear strength steeply increased. This is probably because the recrystallization changes the microstructure of copper wire balls resulting in soften balls. During a ball shear test, first, thick oxide layers formed at the wire surface broke, and the ball fracture occurred. Fig.9 shows the difference of fractured.

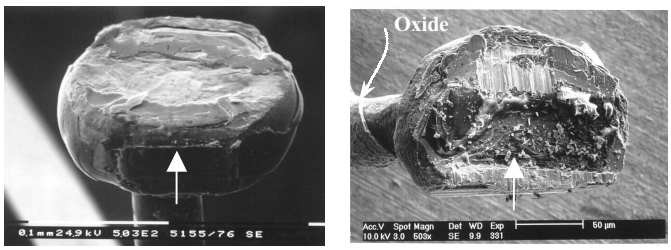

(a) (b)

Fig. 9. SEM images of the bottom of sheared wire balls (a) after annealing at 250°C for 100 hours and (b) at 300°C for 250 hours. The white arrow shows the direction of stylus moving.

balls at 250°C and 300°C. The white arrow indicates where the stylus contacted a ball bond and a sheared direction. Samples, annealed at 250°C, showed a little flattened, but they maintained the original ball shape. However, 300°C of annealing made balls significantly deformed, when they were sheared by stylus. Fig. 9 (b) shows that about 1/4 of a ball was deformed and the contact surface was flattened.

3.4. Micro-XRD analysis

To identify IMC phases, a micro-XRD experiment was performed at the fractured sites after a ball shear test. First of all, micro-XRD was performed on the aluminum pad surface without bonding as a standard reference state. After the shear test of actual bonded samples, IMC phases can be identified by removing standard peaks on the XRD patterns of the fracture sites.

Fractured pad

The XRD patterns of fractured pads after each annealing temperatures, compared with standard peaks, are shown in Fig. 10, Fig. 11, and Fig. 12. At 150°C, (111) Aluminum 1st peak appeared at about 38.5° and others minor peaks occurred from aluminum or SiO_2. IMC peaks were not observed until 50 hours, but after 250 hours, a new peak appeared about 61.5° representing Cu_9Al_4 or CuAl.

Fig. 11. is the XRD results of fractured pads after wires annealed at 250°C. The Cu/Al IMC peak of 61.5° appeared after 250 hours of annealing at 150°C could be observed even after about 25 hours of annealing at 250°C.

Finally, Fig. 12 shows the XRD patterns of 300°C annealed samples. As shown in micro-XRD patterns, it took only 5 hours to form Cu/Al IMC at the interface.

Fractured ball

The XRD results obtained from the bottom of fractured balls, are shown in Fig. 13 and Fig. 14. From the XRD results of fractured pads, Cu/Al IMC phases were confirmed at 250°C sample after 25 hours of annealing. The XRD results of fractured balls are different from those of fractured pads, and the pattern is very complicated because of the overlapping of peaks and background effects. Three phases were identified from this pattern. Aluminum (111) peak is at 38.5° and copper (111) and (200) peaks are at 43.3° and 50.5°. Cu_9Al_4 IMC peaks are 43.9° and 49.6°. This result agrees well with those of XRD results of fractured pads. Therefore, it can be concluded that Cu_9Al_4 is the major forming IMC phase after annealing at 250°C for 25hours.

Similarly, XRD was performed on annealed samples at 300°C for 100 hours. As shown in Fig. 14, Cu_9Al_4 IMC

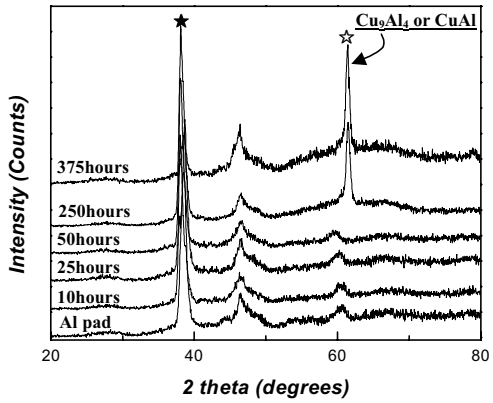

Fig. 10. The micro-XRD patterns of 150°C annealed samples. Micro-XRD experiment was performed at fractured pad sites. (★ : Al, ☆ : Cu_9Al_4 or CuAl)

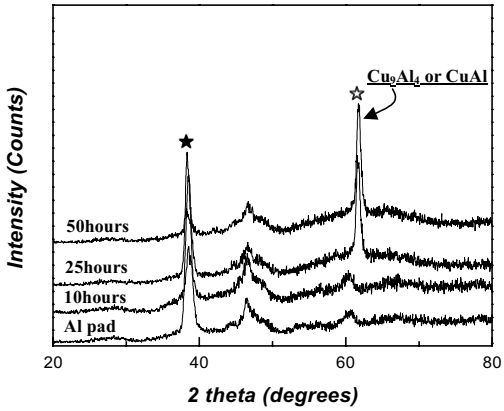

Fig. 11. The micro-XRD patterns of 250°C annealed samples. Micro-XRD experiment was performed at fractured pad sites. (★ : Al, ☆ : Cu_9Al_4 or CuAl)

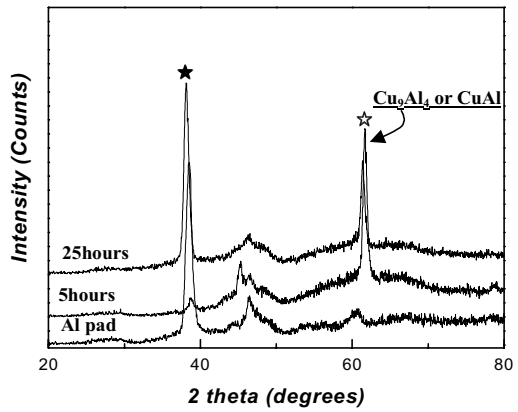

Fig. 12. The micro-XRD patterns of 300°C annealed samples. Micro-XRD experiment was performed at fractured pad sites. (★ : Al, ☆ : Cu_9Al_4 or CuAl)

formed at first as a major IMC. The pattern became more complicated as the annealing time increased because other IMCs such as a $CuAl_2$ formed after longer periods of annealing. Actually, it was difficult to identify exact phases, due to peak split, peak overlapping, and background.

As a summary, in during 150°C to 300°C annealing, major IMC phase was Cu_9Al_4 and other IMC phases formed as annealing times increased.

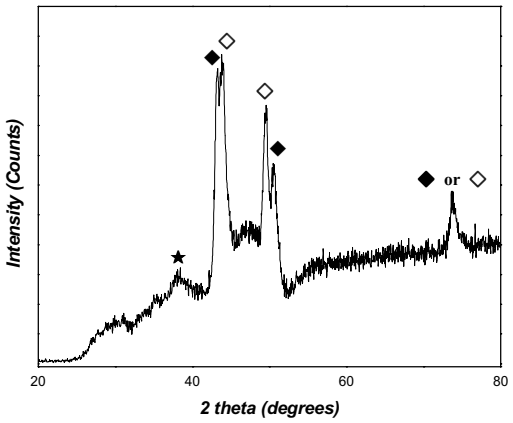

Fig. 13. The micro-XRD patterns of an annealed sample at 250°C for 25 hours. Micro-XRD experiment was performed at the fractured ball site. (★ : Al, ◆ : Cu, ◇ : Cu_9Al_4)

Conclusions

(1) Cu/Al IMC formation was confirmed using SEM and OM when samples were annealed at 150°C to 300°C for 2 hours to 250 hours. Besides, Cu/Al IMC growth follows the parabolic law as a function of annealing times at certain annealing temperature.

(2) The Cu/Al IMC growth is more sensitive to the annealing temperature rather than the annealing time.

(3) The reaction rate of Cu/Al IMC formation was obtained using the Arrhenius plot (lnK vs. 1/T) and the universal IMC growth equation could be derived. Therefore, the theoretical IMC thickness can be calculated as functions

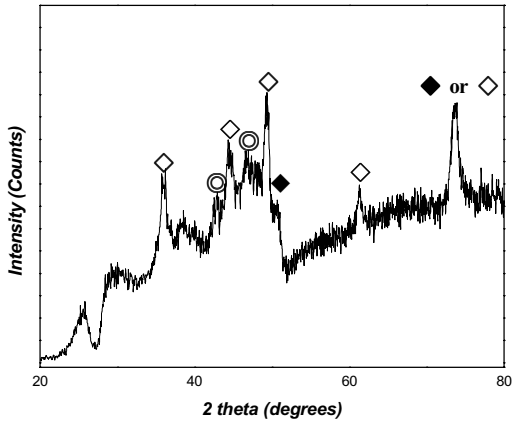

Fig. 14. The micro-XRD patterns of an annealed sample at 300°C for 100 hours. Micro-XRD experiments were performed at the fractured ball site. (◆ : Cu, ◇ : Cu_9Al_4, ◎ : $CuAl_2$)

of time and temperature. Moreover, the reaction rate of Cu/Al IMC formation is 100 times slower than that of Au/Al IMC formation.

(4) The failure mode of ball fracture changed as a function of annealing time. The observed failure modes were the adhesive interface failure (Mode A), the Cu/SiO_2 interface failure (Mode B), the mixed failure (Mode A+Mode B), and the ball inside failure (Mode C) depending on annealing times at 150°C, 250°C, and 300°C, respectively.

(5) The major forming Cu/Al IMC is Cu_9Al_4 at 150 to 300°C annealing. However, more IMC phases were appeared at 300°C for longer annealing time.

References

1. S. Mori, H. Yoshida and N.Uchiyama, "The development of new copper ball bonding-wire," *Proc. 38th Electronic Components Conf.*, 1988, pp.539~545.
2. J.Kurtz, D.Cousens and M. Dufour, "Copper Wire Ball Bonding," *Proc. 34th Electronic Components Conf.*, 1984, pp.1~5.
3. K.Toyozawa, K.Fujita, S.Minamide and T.Maeda, "Development of Copper Wire Bonding Application Technology," *IEEE Trans.-CHMT*, vol. CHMT-13, No. 4 (1990), pp.667~672.
4. M. G.. Osborne, and N. M. Murdeshwar, "Developing Wire Bond Interconnect Solutions for Copper," *3rd Annual Semiconductor Packaging Symposium,* SEMICON West 2000, E-1~E-5.
5. E. Philofsky, "Intermetallic Formation in Gold-Aluminum Systems," *Solid-State Electronics*, vol. 13 (1970), pp.1391~1399.
6. G. V. Clatterbaugh, J. A. Weiner and H. K. Charles, Jr., "Gold-Aluminum Intermetallics :Ball Bond Shear Testing and Thin Film Reaction Couples," *IEEE Trans.-CHMT*, vol. CHMT-7, No. 4 (1984), pp.349~356.

7. Y. Funamizu and K. Watanabe, “Interdiffusion in the Al-Cu System,” *Trans. Japan Inst. of Metal*, vol. 12 (1971), pp.147~152.
8. M. Braunovic and N. Alexandrov, “Intermetallic Compounds at Aluminum to Copper Electrical Interfaces : Effect of Temperature and Electric Current,” *IEEE Trans.-CPMT-A*, vol. 17, No. 1 (1994), pp.78~85.
9. Y. Tamou, J. Li, S. W. Russell and J. W. Mayer, “Thermal and Ion Beam Induced Thin Film Reactions in Cu-Al Bilayers,” *Nuclear Instruments & Methods in Physics Research - Section B*, vol. B64 (1992), pp.130~133.
10. K. Rajan and E. R. Wallach, “A Transmission Electron Microscopy Study of Intermetallic Formation in Aluminum-Copper Thin Film Couples,” *J. of Crystal Growth*, vol. 49 (1980), pp.297~302.

Effects of particle size on dielectric constant and leakage current of epoxy/barium titanate ($BaTiO_3$) composite films for embedded capacitors

Sung-Dong Cho, Joo-Yeon Lee, and Kyung-Wook Paik
Department of Materials Science and Engineering
Korea Advanced Institute of Science and Technology
373-1, Kusong-dong, Yusong-gu, Taejon 305-701, Korea
phone: +84-42-869-3386, fax: +82-42-869-3310
email: chosd1@cais.kaist.ac.kr

Abstract

Polymer/ceramic composite film is of great interest as dielectric material for embedded capacitor applications. In this paper, effects of powder size on dielectric constant and leakage current of epoxy/$BaTiO_3$ composite film fabricated by spin-coating were investigated using bisphenol-A type epoxy and 6 kinds of barium titanate powders with diameter ranges of 0.1~0.9 μm.

Dielectric constant of the composite films increased as particle size increased. This was due to tetragonality increase, which was observed by XRD analysis, with particle size increase. In addition to tetragonality, better dispersibility also contributed to high dielectric constant of bigger powder. Leakage current of composite films increased dramatically as particle size increased. It is presumably due to the decrease of the number of particles per unit length, resulting in decrease of the number of contacts. As the number of contacts acting as a potential barrier reduces, potential barrier lowering effects become larger. When we use larger powder, we can obtain higher dielectric constant with larger leakage current. As a result, there is tradeoff between high dielectric constant and low leakage current, and 0.5 ~ 0.7 μm size powder would be optimum for embedded capacitor applications.

1. Introduction

Electronic systems are composed of lots of electronic components. These components as building blocks are classified by function into active components such as semiconductor and passive components like R, L, and C. Passive components become of increasing interest because the number of the passives is steadily growing as the electronics industry is progressing toward higher functionality. [1] For example the ratio of passive to active components in mobile cellular phone is over 20. [2] Currently these large number of passive components are surface-mounted, so they do not only occupy large area of substrate but also lower electrical performance and reliability due to long interconnection length and increased number of solder joint respectively. To solve these problems, embedded passive technology, which incorporates passive components into multi-layer substrate, has been being actively investigated. Embedded capacitor is of much importance because of large demands and functional importance in electronic circuit like by-pass and decupling capacitors.

Polymer/ceramic composite, which combines processibility of polymer and high dielectric constant of ceramic, is a promising material as embedded capacitor dielectrics, because it uses low-temperature and low-cost process and has compatibility with flexible organic boards. There have been many reports about epoxy/ceramic composite. [3]-[6] However, main concern of many reports has been given to increasing dielectric constant of composite films, and there have been few papers regarding leakage current.

In previous study, [7] we found that dielectric constant and leakage current depend on particle size: bigger powder gives higher dielectric constant with larger leakage current, and vice versa. This paper will present further evidence and explanation for the effects of particle size on dielectric constant and leakage current of epoxy/$BaTiO_3$ composite films using 6 kinds of $BaTiO_3$ powders wiyh different diameter ranging from 0.1 to 0.9 μm.

2. Experimental

2.1. Materials

1) Barium titanate powder and dispersant

Crystal structure of $BaTiO_3$ single crystal is cubic above 120 °C, tetragonal in room temperature, and orthorhombic below 10 °C. $BaTiO_3$ shows paraelectric properties in cubic structure but ferroelectric properties in tetragonal structure. High dielectric constant and ferroelectric properties of $BaTiO_3$ come form the tetragonal structure.

By the way, it is well known that dielectric constant of $BaTiO_3$ strongly depends on grain size or particle size. According to the previous reports, dielectric constant was at its maximum of 5000 when grain size was around 1 ㎛, and decreased drastically as grain size reduced. [8] Origin of the decrease of dielectric constant was attributed to the reduction of tetragonality with decreasing particle size and transition to cubic when powder size was less than 0.12μm. [9] So particle size is very important parameter in selection of powder to get high dielectric constant from it.

In this study, 6 kinds of $BaTiO_3$ powders (Sakai Chemical Industry Co., LTD.) with different particle size ranging 0.1 ~ 0.9 μm were used. Particle size and specific surface area (SSA) are summarized in Table1 and SEM images of the powders with a magnification of ×30000 are shown in Fig.1. As shown in Fig.1, all powders have nearly spherical shape and S-01, S-02, S-03, S-05B, S-04, and S-05 is in order of size from the smallest. Crystal structure of the powders was

Table 1. Characteristics of powders used for this study

Powder #	Particle size (μm)		Spec. surface area (m^2/g) by BET	Dispersant (wt%)
	Nominal	PSA		
S- 01	0.1	0.151	13 ± 3	2.4
S- 02	0.2	0.254	7.1	1.6
S- 03	0.3	0.319	4.0 ± 0.4	2.2
S-05B	0.5	0.752	2.2	1.6
S- 04	0.4	0.832	2.4	1.6
S- 05	0.5	0.916	2.3	1.4

(Ba/Ti ratio: 0.999 ± 0.003, PSA: particle Size Analysis, These are based on the data provided by manufacturers)

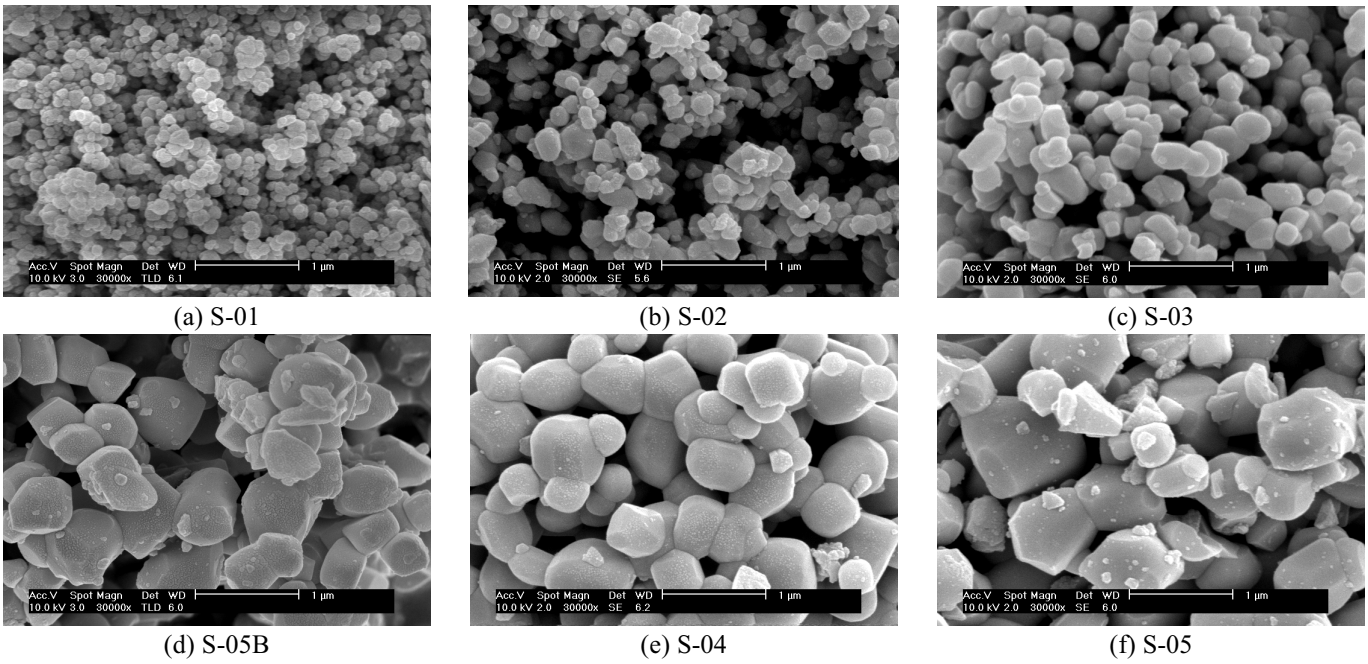

(a) S-01 (b) S-02 (c) S-03

(d) S-05B (e) S-04 (f) S-05

Fig. 1 SEM images of $BaTiO_3$ powders used for the study

investigated by X-ray diffraction (XRD) analysis using Cu K-α line.

Phosphate ester (BYK Chemie) was used as dispersant of BaTiO3 powder. To determine the amount of dispersant for each powder, we measured viscosity of suspension containing powder, dispersant, and solvent as a function of dispersant amount. And the value at which viscosity was minimized was chosen. The values are also shown in Table 1.

2) Epoxy, curing agent and solvent

Bisphenol-A epoxy (E.E.W.; 5,000~6,000) was used as matrix polymer. Dicyandiamide (DICY) was used as curing agent, because it's curing onset temperature is so high that curing does not progress in room temperature and pot life is long. Quantity of DICY added was 10wt% of epoxy weight. Propylene glycol monomethyl ether acetate (PGMEA; b.p. 146°C) was used as solvent.

2.2. Epoxy/$BaTiO_3$ composite capacitor fabrication

Metal-Insulator-Metal (MIM) capacitors was fabricated on Si-wafers. The fabrication procedure is as follows. The dispersant was dissolved into the solvent and then the powders were dispersed into that solution, and ball milling was performed for 2 days. After that, the epoxy was added to this slurry and another ball milling was performed for 1 day. The suspension was spin-coated (2000 and 4000 rpm-30sec) on the Si-wafers on which aluminum blanket (0.5 ㎛) had been deposited for bottom electrode. After drying it in the condition of 110℃ and 1 hour in vacuum oven, film curing was done at 200°C for 30 min. Using shadow mask, aluminum top electrodes of circle shape (thickness: 0.5 ㎛, area: 0.1257cm^2) were deposited by sputtering method. Powder loading of the composite films was 67 vol%.

2.3. Capacitor characterization

Thickness of the composite film was measured using surface profilemeter (Alpha-step). Capacitance and dielectric loss were measured at 100kHz by using HP 4284A LCR meter.

Table 2. Measured values of properties of epoxy/$BaTiO_3$ composite capacitors with various powders

Powder	Coating speed (rpm)	Thickness (μm)	Capacitance (nF/cm^2)	Dielectric loss
S- 01	2000	4.249	9.014	0.0225
	4000	2.403	15.75	0.0239
S- 02	2000	4.253	10.84	0.0228
	4000	2.720	14.96	0.0218
S- 03	2000	4.500	11.65	0.0232
	4000	2.873	16.95	0.0236
S- 05B	2000	4.192	13.37	0.0214
	4000	2.725	21.30	0.0257
S- 04	2000	4.352	13.24	0.0266
	4000	3.761	18.46	0.0253
S- 05	2000	3.740	14.81	0.0229
	4000	2.550	22.08	0.0241

Dielectric constant was computed from thickness and capacitance data. Leakage current was measured by using Keithley 236 Source Measure Unit. Bias was applied up to 0.1 MV/cm according to each film thickness and current values at 10V and 0.1MV/cm were recorded.

3. Results and discussion

3.1. Dielectric constant and particle size

Average values of thickness, capacitance, and dielectric loss of the composite capacitors fabricated with 6 different powders are summarized in Table 2. According to coating speed and given powders, 2.5 ~ 4.5 μm thick films were deposited. Capacitance was within 9 ~ 20 nF/cm^2 and dielectric loss was less than 0.03 in all samples. Dielectric constant calculated from thickness and capacitance is shown in Fig. 2. It increased as particle size increased and saturation occurred over S-05B.

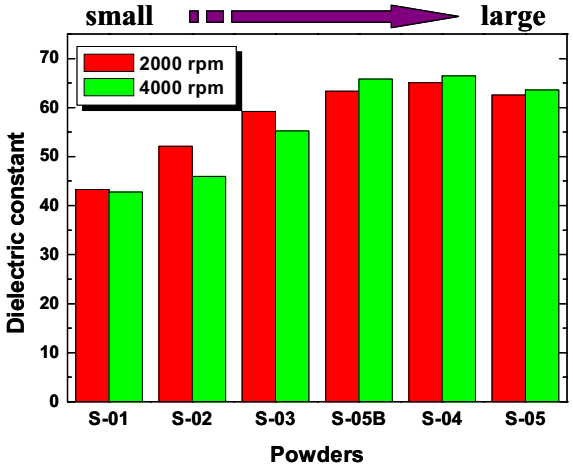

Fig. 2 Dielectric constant of epoxy/$BaTiO_3$ composite capacitor fabricated with various powders

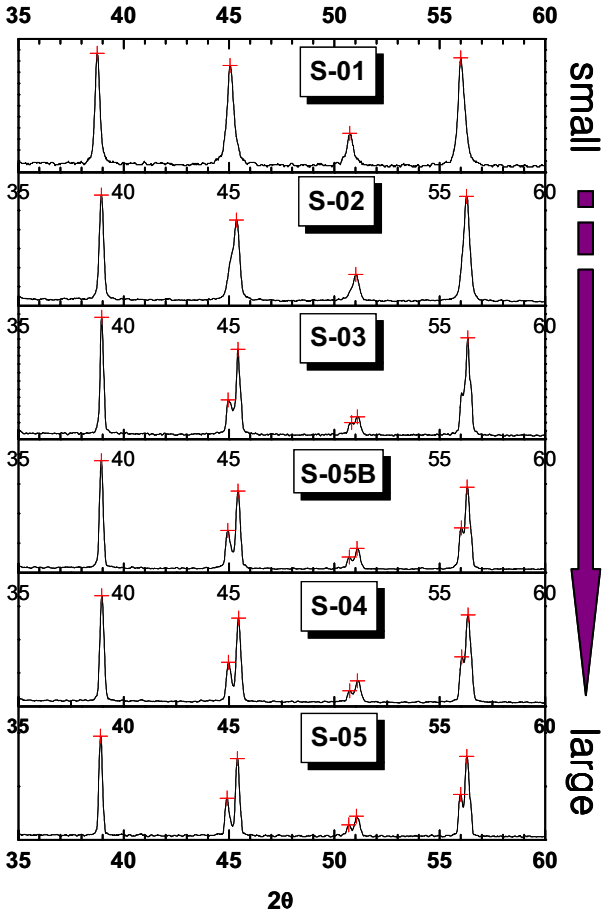

Fig. 3 XRD pattern of the powders as a function of 2θ ranging from 35° to 60°

To understand this result, crystal structure and dispersibility of each powder were investigated. Fig. 3 is XRD patterns of the 6 powders within 2θ ranging 35°~ 60°.

Tetragonal structure can be distinguished from cubic structure with {200} reflection around 45°. Split of {200} reflection into (002) and (200) peaks occurs in tetragonal but not in cubic structure. We cannot find the peak split in the smallest powder S-01. But over S-03, two peaks were observed clearly as shown in Fig. 3. In case of S-02, peak split was not clear. But it is supposed that two peak positions are close and overlapped each other. To quantify degree of tetragonality, {200} reflection was magnified (Fig. 4) and difference between (002) and (200) peak position (Δ2θ) was measured because tetragonality is proportional to Δ2θ. Result is shown in Fig. 5. Δ2θ increased as powder size increased as shown in Fig. 5. This tendency coincided with the tendency of dielectric constant found in Fig.2. So, increase of dielectric constant with increasing particle size is mainly due to increase of tetragonality of powder.

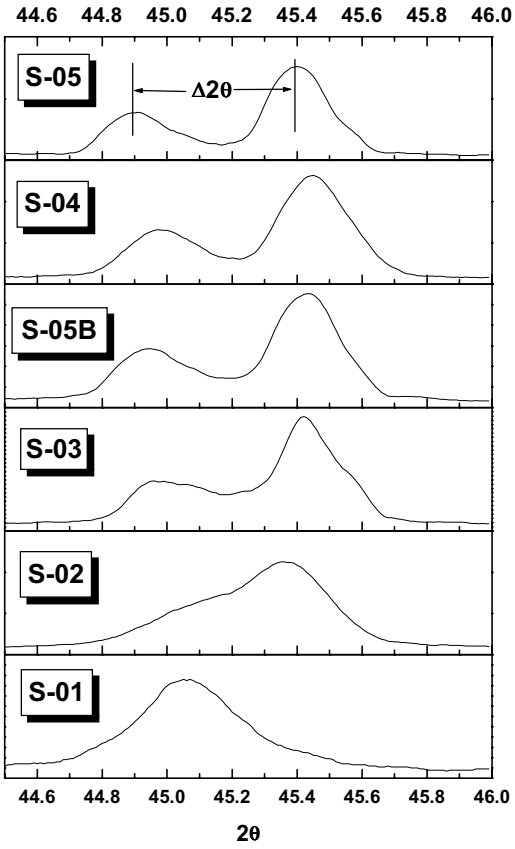

Fig. 4 X-ray {200} reflection of the powders

Fig. 6 shows viscosity of suspension containing each powder (volume loading: 33.3vol%). Viscosity of the suspensions decreased as particle size increased. This means better dispersion at larger particle size. When the same amount of powder is used, higher dielectric constant is obtained at better dispersion condition. This is due to reduction of number of agglomerates, which can trap pore or solvent that lowers dielectric constant of film. [10] So it is thought that better dispersion with increasing particle size also helped the increase of dielectric constant.

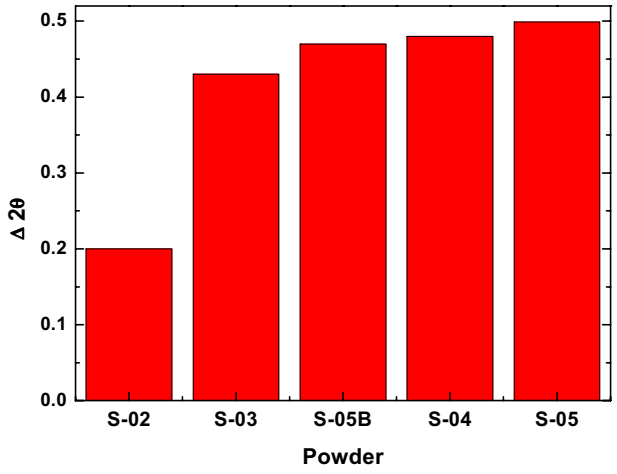

Fig. 5 Difference between (002) peak and (200) peak positions (Δ2θ)

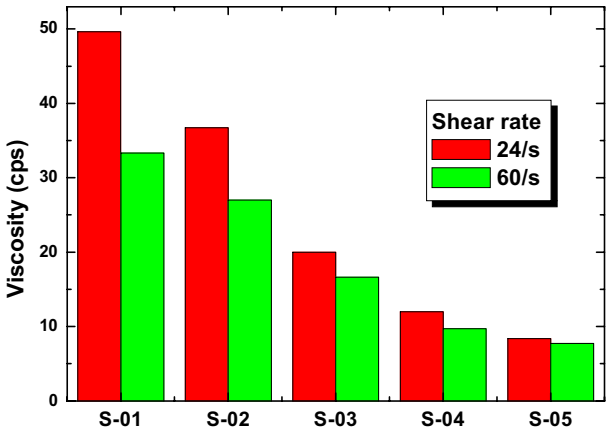

Fig. 6 Minimum viscosity of each powder at shear rate of 24/s and 60/s

In conclusion, higher tetragonality and better dispersibility of large powder increased the dielectric constant of the epoxy/$BaTiO_3$ composite capacitor.

3. 2. Leakage current and particle size

Fig.7 (a) and (b) show leakage current of the composite capacitors at 0.1 MV/cm and 10 V respectively as a function of powder size. Comparing the leakage current of the 6 powders from Fig. 7 (a), it was found that leakage current increased dramatically with increasing particle size. In practical point, requirement of leakage current is to be less than 10^{-6} A/cm^2 at 10V. So from the Fig. 7 (b), S-04 and S-05 cannot be used as embedded capacitor material because leakage current is too high at a given film thickness.

I-V characteristics were investigated to find out the cause of the large leakage current of large powder. Fig. 8 shows I-V behaviors of S-01 and S-05 composite films. I-V behaviors of two powders were very different. In case of S-01 leakage

current was very low and it seemed that conduction was by Schottky emission mechanism. In case of S-05, however, leakage current was very high and it appeared that Ohmic conduction was dominant.

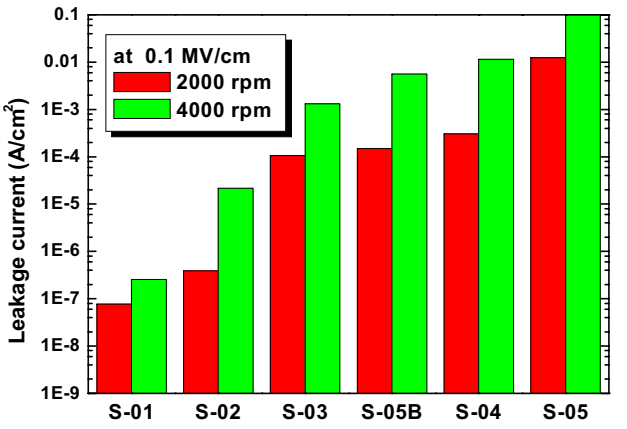

(a)

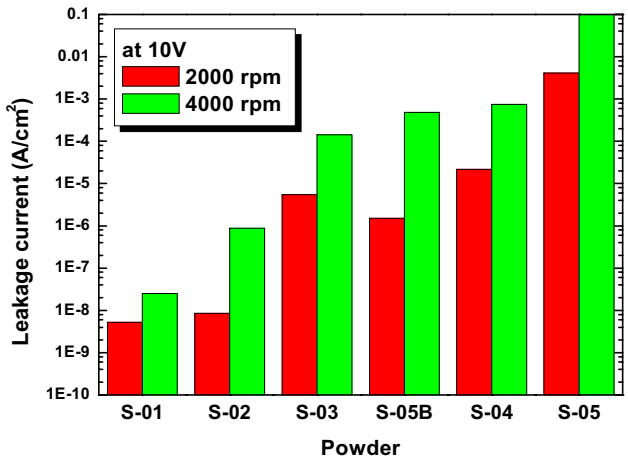

(b)

Fig. 7 Leakage current of the epoxy/$BaTiO_3$ composite capacitors with the various powders at (a) 0.1 MV/cm and (b) 10 V

Magnitude of leakage current can be correlated with the number of particle per unit length to explain the difference. As shown in Fig. 9, the number of particles and contacts per unit length decreases as particle size increases. It is thought that powder surface is more conductive than powder bulk and polymer matrix, presumably because on powder surface lots of defects exist and dispersant is adsorbed as ion. Therefore, it is likely that conduction path in epoxy/$BaTiO_3$ composite film would be powder surface, and contacts between particles act as resistance or potential barrier. So primary origin of high leakage current of large powder is due to the decrease of the number of contacts per unit length with increasing particle size.

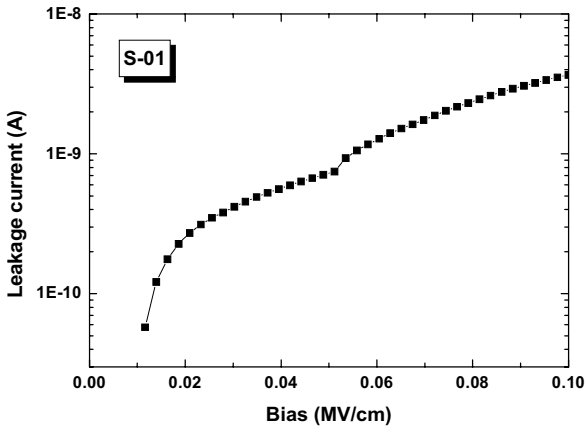

(a)

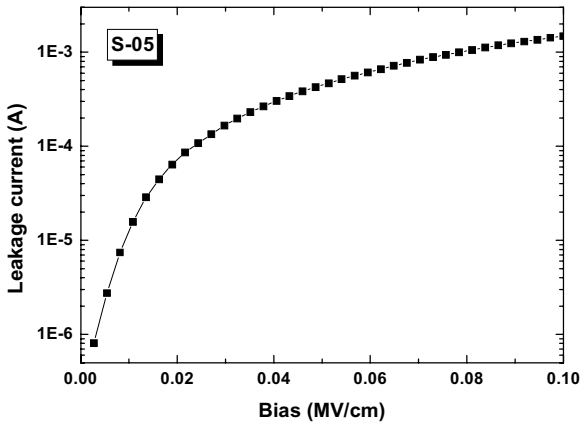

(b)

Fig. 8 Leakage current behaviors of (a) S-01 and (b) S-05

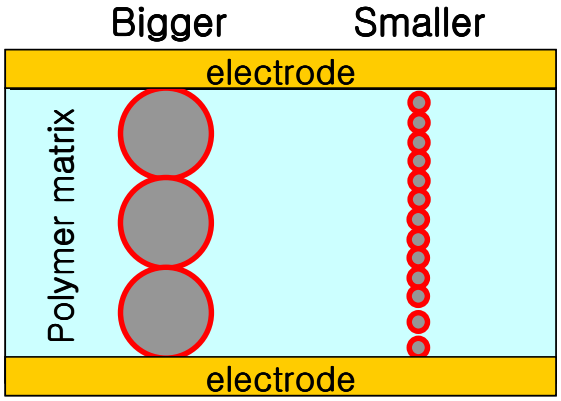

Fig. 9 Leakage current model; difference of the number of contact per unit length between bigger powder and smaller powder

In addition, since decrease of the number of contacts makes the bias applied per one contact so larger and potential barrier lowering effects stronger, leakage current increases

much more. The reason that the Schottky barrier disappeared and the Ohmic conduction appeared in S-05 is due to the increase of bias applied per one contact at the same electric field; the bias was so large that potential barrier disappeared

4. Conclusion

Epoxy/$BaTiO_3$ composite capacitors were fabricated using 6 different size $BaTiO_3$ powders, and effects of particle size on dielectric constant and leakage current of the composite capacitors were investigated. Dielectric constant increased with increasing particle size. It was mainly due to increase of dielectric constant of powders resulted from increase of tetragonality. Better dispersion also contributed. Leakage current increased as particle size increased. This large increase of leakage current is presumably due to decrease of the number of particles and contacts per unit length, which act as potential barrier, and increase of barrier lowering effect per contact.

From the results, in case of $BaTiO_3$ powder less than 1μm, higher dielectric constant can be obtained at larger particle size. But large powder has disadvantage of large leakage current. Therefore, trade-off between dielectric constant and leakage current when selecting powder is necessary. According to our results, proper particle size for uses for embedded capacitors is 0.5 ~ 0.7 μm in diameter.

5. Acknowledgement

This work was supported by Center of Electronic Packaging Materials of Korea Science and Engineering Foundation.

6. References

1. J. Prymark, *et al.,* "Fundamentals of Passives: Discrete, Integrated, and Embedded", Chap. 11 in Fundamentals of Microsystems Packaging, ed. by R. R. Tummala, McGraw-Hill, (New York, 2001), pp. 420
2. J. Rector, "Economic and Technical Viability of Integral Passives", in *Proc. of 48th Electronic Components and Technology Conf.*, Seattle, WA, May, 1998, pp. 218-224
3. S. K. Bhattacharya and R. R. Tummala, "Next Generation Integral Passives: Materials, Processes, and Integration of Resistors and Capacitors on PWB sybstrates," *J. Mater. Sci: Materials in Electronics*, Vol. 11, No. 3 (2000), pp. 253-268
4. S. Ogitani, S. A. Bidstrup-Allen, and P.A. Khol, "Factors Influencing the Permittivity of Polymer/Ceramic Composite for Embedded Capacitors", *IEEE Trans. on Advanced Packaging*, Vol. 23, No.2 (2000), pp.313-322
5. B. A. Schutzberg, *et al.*, "Integral Thin Film Capacitors: Materials, Performance and Modeling", in *Proc. of 50th Electronic Components and Technology Conf.*, Las Vegas, NV, May, 2000, pp. 1564-1567
6. Y. Rao, *et al.*, "Novel high Dielectric Constant Nano-structure Polymer-ceramic Composite for Embedded Capacitor Application", in *Proc. of 50th Electronic Components and Technology Conf.*, Las Vegas, NV, May, 2000, pp. 183-187
7. S. D. Cho and K. W. Paik, "Relationship between Suspension Formulations and the Properties of $BaTiO_3$/Epoxy Composite Films for Integral Capacitors", in *Proc. of 51st Electronic Components and Technology Conf.*, Orlando, FL, May, 2001, pp. 1418-1422
8. G. Arlt, D. Henning, and G. de With, "Dielectric properties of fine-grained barium titante ceramics," *J. Appl. Phys.* Vol. 58, No. 4 (1985), pp. 1619-1625
9. K. Uchino, E. Sadanaga, and T. Hirose, "Dependence of Crystal Structure on Particle Size in Barium Titanate," *J. Am. Ceram. Soc.*, Vol. 72, pp. 1555-1558
10. V. Agarwal, et al, "Improvements and Recent Advances in Nanocomposite Capacitors Using a Colloidal Technique", in *Proc. of 48th Electronic Components and Technology Conf.*, Seattle, WA, May, 1998, pp. 165-170